



Review

The stability of sulfate and hydrated sulfate minerals near ambient conditions and their significance in environmental and planetary sciences

I-Ming Chou ^{a,*}, Robert R. Seal II ^a, Alian Wang ^b^a U.S. Geological Survey, 954 National Center, Reston, VA 20192, USA^b Department of Earth and Planetary Sciences and McDonnell Center for Space Sciences, Washington University, St. Louis, MO 63130, USA

ARTICLE INFO

Article history:

Received 7 February 2012

Received in revised form 5 November 2012

Accepted 12 November 2012

Available online 28 November 2012

Keywords:

Metal sulfate

Hydrated sulfate minerals

Humidity and temperature

Thermodynamics and kinetics

Terrestrial occurrence

Planetary occurrence

ABSTRACT

Sulfate and hydrated sulfate minerals are abundant and ubiquitous on the surface of the Earth and also on other planets and their satellites. The humidity-buffer technique has been applied to study the stability of some of these minerals at 0.1 MPa in terms of temperature–relative humidity space on the basis of hydration–dehydration reversal experiments. Updated phase relations in the binary system $\text{MgSO}_4\text{--H}_2\text{O}$ are presented, as an example, to show how reliable thermodynamic data for these minerals could be obtained based on these experimental results and thermodynamic principles. This approach has been applied to sulfate and hydrated sulfate minerals of other metals, including Fe (both ferrous and ferric), Zn, Ni, Co, Cd, and Cu.

Metal–sulfate salts play important roles in the cycling of metals and sulfate in terrestrial systems, and the number of phases extends well beyond the simple sulfate salts that have thus far been investigated experimentally. The oxidation of sulfide minerals, particularly pyrite, is a common process that initiates the formation of efflorescent metal–sulfate minerals. Also, the overall abundance of iron-bearing sulfate salts in nature reflects the fact that the weathering of pyrite or pyrrhotite is the ultimate source for many of these phases. Many aspects of their environmental significance are reviewed, particularly in acute effects to aquatic ecosystems related to the dissolution of sulfate salts during rain storms or snow-melt events.

Hydrous Mg, Ca, and Fe sulfates were identified on Mars, with wide distribution and very large quantities at many locations, on the basis of spectroscopic observations from orbital remote sensing and surface explorations by rovers. However, many of these findings do not reveal the detailed information on the degree of hydration that is essential for rigorous interpretation of the hydrologic history of Mars. Laboratory experiments on stability fields, reactions pathways, and reaction rates of hydrous sulfates likely to be found on Mars enhance our understanding of the degrees of hydration of various sulfates that should currently exist on Mars at various seasons and locations and during various atmospheric pressure and obliquity periods. Two sets of systematic experiments were described; one on hydrous Mg sulfates and the other on hydrous Fe^{3+} sulfates. Also, their implications to Mars sulfates mineralogy were discussed.

Published by Elsevier Ltd.

Contents

1. Introduction	735
2. The humidity buffer technique	735
3. Phase relations and thermodynamics in the system $\text{MgSO}_4\text{--H}_2\text{O}$ – an example	736
4. Stability of sulfate and hydrated sulfate minerals of other metals	739
5. Terrestrial metal–sulfate efflorescent salts	739
5.1. High temperature settings	739
5.2. Low temperature settings	740
5.2.1. Mineralogy	740
5.2.2. Processes of formation	742

* Corresponding author. Tel.: +1 703 6486169; fax: +1 703 6486252.

E-mail address: imchou@usgs.gov (I-M. Chou).

5.2.3. Occurrences	744
5.2.4. Environmental significance	745
6. Stability field, phase transition pathways, and reaction rates of hydrous sulfates under the conditions relevant to Mars	746
6.1. Occurrence of Martian sulfates	746
6.2. Experiments on the stability field, phase transition pathways, and reaction rates of Mg-sulfates	747
6.2.1. Experiments in three stages	747
6.2.2. Results and discussions	748
6.3. Experiments on the stability field, phase transition pathways, and phase boundaries of Fe ³⁺ sulfates	751
6.3.1. Experiments in three stages	751
6.3.2. Results and discussions	751
7. Future research	755
Acknowledgments	755
References	755

1. Introduction

Simple hydrated metal–sulfate salts, such as epsomite (MgSO₄·7H₂O), coquimbite (Fe₂³⁺(SO₄)₃·9H₂O), and halotrichite (Fe²⁺Al₂(SO₄)₄·22H₂O), where one or more cations combine with sulfate and a number of waters of hydration, have received an explosion of scientific attention over the past one to two decades. Two main reasons are responsible for this focused attention. First, they form at the surface of the Earth through the weathering of sulfide minerals, where they can sequester or store metals and acidity in a highly soluble form during dry periods; these minerals can dissolve readily during rain events or spring snow melt, causing acute toxic events such as fish kills downstream (Nordstrom, 2009). Second, spectral data from satellites orbiting Mars or more recently from rovers on the Martian surface have identified magnesium and iron sulfate salts as important constituents of the Martian soil, where they likely play important roles in the hydrologic cycle of the planet and represent clues in the search for evidence of life on the planet (Squyres et al., 2004). Similarly, orbital remote sensing studies of other planets and their satellites, such as the Jovian moon Europa, have indicated the presence of these phases elsewhere in the solar system (Chou and Seal, 2003a; Dalton et al., 2012).

The crystallography, geochemistry, and environmental significance of sulfate and hydrated sulfate minerals, which are abundant and ubiquitous in the lithosphere of Earth and also on other planets and their satellites, were last reviewed comprehensively over a decade ago (i.e., Alpers et al., 2000). In 2000, information on the stability of sulfate and hydrated sulfate minerals and their thermodynamic and kinetic properties were lacking due to limited experimental observations and reliable measurements. Thus, one of the greatest obstacles to improving of understanding of the behavior of these minerals in both terrestrial and extraterrestrial environments was the lack of reliable thermodynamic data for these phases and the lack of adequate kinetic data for the rates of reactions among these phases.

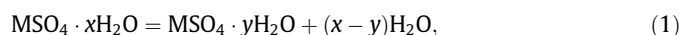
The purpose of this review paper is to summarize recent laboratory studies related to the thermodynamic and kinetic properties of this group of minerals as they relate to surface environment on Earth and Mars. Temperature and relative humidity (RH) are master variables that determine the stability of many of these minerals under a range of conditions. The humidity-buffer technique, which has formed the basis of much of the recent experimental research on these phases, is described (Chou et al., 2002). This paper also summarizes the occurrences of metal–sulfate minerals in terrestrial settings, particularly those associated with mining. Experimental studies related to the stability and reaction rate of these phases under conditions relevant to Mars and its hydrologic cycle are described.

These minerals present a number of challenges in terms of preservation from the time of collection in the field to the time of analysis and characterization due to their rapid rates of hydration, dehydration, and oxidation for those containing ferrous iron and other reduced elements. A review of these topics is beyond the scope of this paper. Instead, the reader is referred to recent comprehensive studies by Frost et al. (2006) and Hyde et al. (2011) for pertinent information. Furthermore, less soluble and reactive simple sulfate minerals such as anglesite (PbSO₄) and barite (BaSO₄), and hydroxysulfates such as schwertmannite (Fe³⁺O₈(OH)_{8–2x}·(SO₄)_x·nH₂O where 1 ≤ x ≤ 1.75), jarosite ((K, Na, H₃O)Fe₃³⁺(SO₄)₂(OH)₆), and alunite ((K, Na)Al₃(SO₄)₂(OH)₆), among others, are beyond the scope of this review and are only mentioned as needed for completeness in describing mineral assemblages despite their geologic importance.

2. The humidity buffer technique

The humidity-buffer technique was based on the isopiestic method, which was widely used for the determination of solvent activity of nonvolatile solutions (e.g., Pytkowicz, 1979; Clegg and Whitfield, 1991; Barthel et al., 1998). The humidity-buffer technique was developed by Polyanskii et al. (1976) for the study of ion-exchange resins, and later used by Malinin et al. (1977), Chou et al. (2002), Jerz and Rimstidt (2003), Vaniman et al. (2004), Vaniman and Chipera (2006), Kong et al. (2011a), Wang et al. (2009, 2011), and Chou and Seal (2003a, 2003b, 2004, 2005a, 2005b, 2007) for the stability studies of metal sulfate and hydrated metal sulfate minerals. This technique has also been used for mineral characterization (Anderson et al., 2007), monitoring phase transition in real-time (Peterson and Grant, 2005), and development of microanalytical techniques (Hyde et al., 2011). After comparing the humidity-buffer technique with the gas-flow-cell method, which was designed by Parkinson and Day (1981) to control precisely the RH for plant growth experiments, Chou et al. (2002) preferred the humidity-buffer technique for their mineral stability studies because of better temperature control and more precise reversibility.

For the hydration–dehydration reaction of the sulfate minerals of a divalent metal M:



$$\begin{aligned} \Delta G_r^\circ &= -RT \ln K = -(x - y)RT \ln(a\text{H}_2\text{O}) \\ &= -(x - y)RT \ln(f\text{H}_2\text{O}/0.1) \\ &= -(x - y)RT \ln[(f^* \text{H}_2\text{O}/0.1) \cdot (\%RH)/100], \end{aligned} \quad (2)$$

where x and y are the numbers of water molecules per formula of the minerals, ΔG_r[°] is the standard Gibbs free energy of reaction for

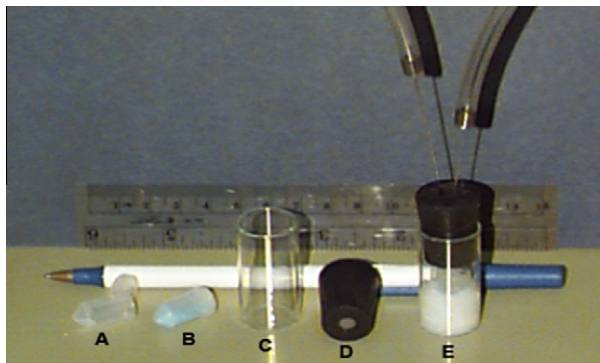


Fig. 1. Experimental setup for the humidity buffer experiments. (A) Plastic sample capsule having a cap with several small holes. (B) Sample in the capsule. (C) Glass container. (D) A rubber stopper with a septum. (E) A sample capsule was partially immersed in a humidity buffer in a glass container sealed by the rubber stopper. Two needles penetrated through the septum were used to replace air in the headspace by nitrogen to minimize oxidation for samples containing Fe^{2+} . The ruler shows 15 cm scales at top and 6 in. scales at bottom.

reaction (1), K is the equilibrium constant, R is the gas constant ($8.31451 \text{ J mol}^{-1} \text{ K}^{-1}$); T is absolute temperature; $a_{\text{H}_2\text{O}}$ is the activity of H_2O ; $f_{\text{H}_2\text{O}}$ is the equilibrium H_2O fugacity (in MPa); and $f^{\circ}\text{H}_2\text{O}$ is the fugacity of water (in MPa) at T . The standard states for minerals and H_2O are pure solids and H_2O , respectively, at 0.1 MPa and temperature. Here RH is defined as:

$$RH = (f_{\text{H}_2\text{O}}/0.1)/(f^{\circ}\text{H}_2\text{O}/0.1). \quad (3)$$

To determine the equilibrium constant K for reaction (1) at a fixed T , according to Eq. (2), we only need to measure the equilibrium $\%RH$ for this reaction, because $f^{\circ}\text{H}_2\text{O}$ is well known and can be obtained from a steam table (e.g., Haar et al., 1984). The humidity-buffer technique is the most convenient and reliable way to obtain the equilibrium $\%RH$, and the experimental setup used by Chou et al. (2002) is shown in Fig. 1.

A weighed amount of sample, a roughly 1:1 mixture of reactant and product minerals (typically 100–250 mg), was loaded into a plastic sample container (A in Fig. 1; 8 mm ID \times 10 mm OD and 20 mm tall), which was partially immersed in a humidity buffer, consisting of a binary saturated solution (Fig. 2; Greenspan, 1977) in a glass container (C in Fig. 1; 17.5 mm ID \times 20 mm OD and 40 mm tall) sealed by a rubber stopper with a septum (D in Fig. 1). Small holes through the cap of the sample chamber allowed the vapor phase of the sample to equilibrate with that of the buffer

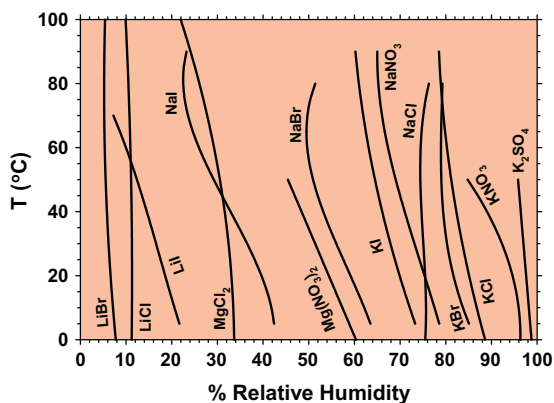


Fig. 2. Selected humidity buffers from 28 binary saturated aqueous solutions reported by Greenspan (1977) for relative humidities from 3% to 98% at 0.1 MPa. Uncertainties in predicted $\%RH$ can be as much as ± 2.9 , but mostly are less than ± 0.6 .

system at a fixed temperature. To minimize oxidation for experiments containing Fe^{2+} , the air in the headspace of the sample-buffer system was replaced by nitrogen by the use of two needles penetrated through the septum (E in Fig. 1). The whole assembly was then immersed in a water bath, the temperatures of which were controlled to $\pm 0.03 \text{ }^{\circ}\text{C}$ and measured by using a Pt resistance probe (accurate to $\pm 0.02 \text{ }^{\circ}\text{C}$). The durations of experiment after each temperature change are at least 10 h, and more than 24 h in most cases, to make sure the system reaches osmotic equilibrium (see Fig. 6 of Chou et al., 2002). The direction of reaction was determined by the sample mass change (precise to $\pm 0.05 \text{ mg}$). Both starting material and experimental products were examined by using X-ray diffraction and optical methods (including Raman spectroscopy) to make sure that no unexpected phases were formed. According to Greenspan (1977), uncertainties in predicted $\%RH$ for the humidity buffers used in the temperature range of most of our studies are no more than $\pm 0.6\%$.

3. Phase relations and thermodynamics in the system $\text{MgSO}_4\text{--H}_2\text{O}$ – an example

We present the updated phase relations among the well-studied sulfate and hydrated sulfate minerals in the system $\text{MgSO}_4\text{--H}_2\text{O}$, as an example, to show (1) how in recent years we have minimized the uncertainties associated with the stability of these minerals, and (2) how to obtain reliable thermodynamic data for these minerals by using the humidity buffer technique and the thermodynamic principles.

Minerals in the system $\text{MgSO}_4\text{--H}_2\text{O}$ include kieserite ($\text{MgSO}_4 \cdot \text{H}_2\text{O}$), starkeyite ($\text{MgSO}_4 \cdot 4\text{H}_2\text{O}$), cranswickite ($\text{MgSO}_4 \cdot 4\text{H}_2\text{O}$; Peterson, 2011), hexahydrate ($\text{MgSO}_4 \cdot 6\text{H}_2\text{O}$), epsomite ($\text{MgSO}_4 \cdot 7\text{H}_2\text{O}$), and meridianiite ($\text{MgSO}_4 \cdot 11\text{H}_2\text{O}$; Peterson et al., 2007). Their stability relations are summarized in Fig. 3 (modified from Fig. 1 of Chou and Seal, 2007) as a function of T and composition (mass% of MgSO_4) in the $\text{MgSO}_4\text{--H}_2\text{O}$ binary system at 0.1 MPa. Note that the field of $\text{MgSO}_4 \cdot 12\text{H}_2\text{O}$ reported by Hogenboom et al. (1995) was replaced by $\text{MgSO}_4 \cdot 11\text{H}_2\text{O}$ based on the report of Peterson and Wang (2006) and that $\text{MgSO}_4 \cdot 6\text{H}_2\text{O}$ is not stable below $11 \text{ }^{\circ}\text{C}$ (Chou and Seal, 2003a). Also note that the stability field for the newly discovered cranswickite is still not determined. The plotted

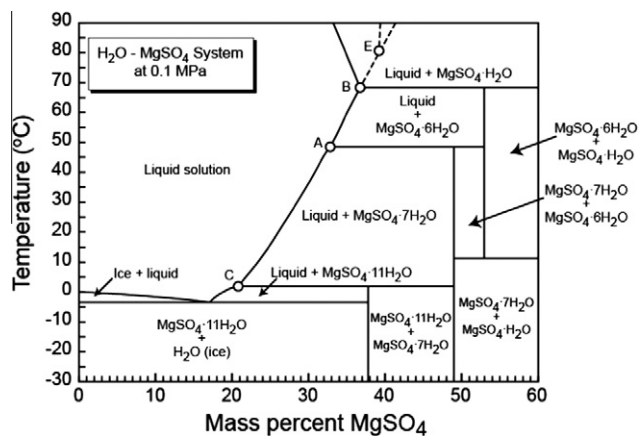


Fig. 3. Phase diagram for the system $\text{MgSO}_4\text{--H}_2\text{O}$ at 0.1 MPa. Note that the field of $\text{MgSO}_4 \cdot 12\text{H}_2\text{O}$ reported by Hogenboom et al. (1995) was replaced by $\text{MgSO}_4 \cdot 11\text{H}_2\text{O}$ based on the report of Peterson and Wang (2006) and that $\text{MgSO}_4 \cdot 6\text{H}_2\text{O}$ is not stable below $11 \text{ }^{\circ}\text{C}$ (Chou and Seal, 2003a). The points A, B, C, and E are isobaric invariant points for the assemblages epsomite–hexahydrate–aqueous solution–vapor (EHAV), hexahydrate–kieserite–aqueous solution–vapor (HKAV), meridianiite–epsomite–aqueous solution–vapor (MEAV), and hexahydrate–starkeyite–aqueous solution–vapor (HSAV), respectively. The isobaric invariant point E, which is in the stability field of liquid + $\text{MgSO}_4 \cdot \text{H}_2\text{O}$, is metastable.

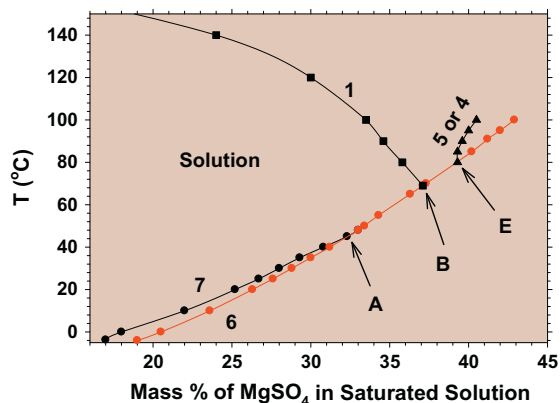
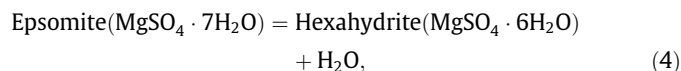


Fig. 4. Solubilities of epsomite (7; black dots and connected curve), hexahydrate (6; red dots and connected curve), pentahydrate (5; black triangles and connected curve), starkyite (4; black triangles and connected curve), and kieserite (1; black squares and connected curve) in water at 0.1 MPa compiled by Linke and Seidell (1965). A, B, and E are the isobaric invariant points described in Fig. 3.

composition of mineral-saturated solution at a specific T was based on the mineral solubility data (Fig. 4). For example, curve AB in Fig. 3 was based on the solubility data of hexahydrate in water (red curve in Fig. 4) summarized by Linke and Seidell (1965). The solubility of these minerals increases with increasing T , except kieserite (black squares and connected curve shown in Fig. 4). Points A, B, and C in Fig. 3 are isobaric invariant points for the assemblages of epsomite–hexahydrate–aqueous solution–vapor (EHAV), hexahydrate–kieserite–aqueous solution–vapor (HKAV), and meridianiite–epsomite–aqueous solution–vapor (MEAV), respectively. The isobaric invariant point E, which is in the stability field of liquid + $\text{MgSO}_4 \cdot \text{H}_2\text{O}$, is for the metastable assemblage hexahydrate–starkyite–aqueous solution–vapor (HSAV; Chou and Seal, 2007). No solubility data have been reported for meridianiite, but the T of the invariant point C was determined to be at 2 °C (Peterson and Wang, 2006).

There is one more important parameter/variable that we need to consider when we discuss the stability of these minerals, the vapor pressure of H_2O or relative humidity (RH), especially in the absence of an aqueous phase in the system, such as the stability of individual minerals as a function of T and RH within the stability field of epsomite + hexahydrate shown in Fig. 3.

For the reaction



$$\begin{aligned} \Delta G_r^\circ &= -RT \ln K = -RT \ln(a_{\text{H}_2\text{O}}) = -RT \ln(f_{\text{H}_2\text{O}}/0.1) \\ &= -RT \ln[(f^*_{\text{H}_2\text{O}}/0.1) \cdot (\%RH)/100], \end{aligned} \quad (5)$$

The stability of epsomite and hexahydrate under the air at 0.1 MPa pressure, in the presence or absence of an aqueous phase, can be represented by a diagram using T and %RH as two variables (Fig. 5; modified from Fig. 1 of Chou and Seal, 2003a). In Fig. 5, we show the equilibrium stability boundary between epsomite and hexahydrate based on the thermodynamic data compiled by Wagman et al. (1982; blue curve) and DeKock (1986; red curve), and also based on experimental vapor pressure measurements. The boundary reported by Chou and Seal (2003a), shown here by the black dashed curve, is based on the reversal points along four humidity buffer curves listed in Table 1 (red circles along the NaBr, KI, NaCl, and KBr buffer curves). For example, the experimental results along the KBr buffer curve are shown in Fig. 6 and the reversal point is at 44.18 ± 0.38 °C (red circle on KBr buffer curve shown in

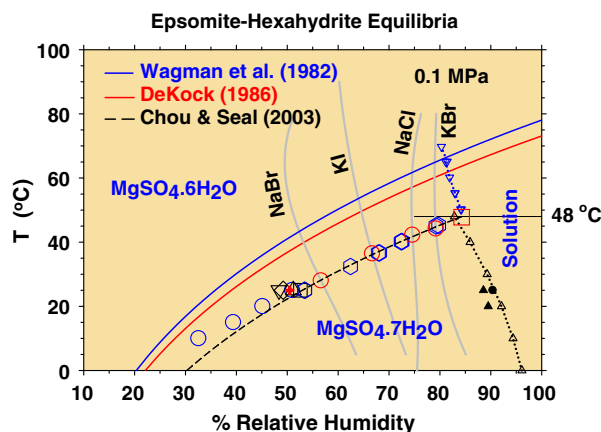


Fig. 5. Epsomite–hexahydrate equilibria at 0.1 MPa. Results of vapor pressure measurements at 0.1 MPa and 25 °C are shown by the large black triangle with the apex pointing up (Frowein, 1887), the diamond (Lescoeur, 1889), the large triangle with the apex pointing down (Foote and Scholes, 1911), the red plus sign (Bolte, 1912), and the square (Schumb, 1923). Those between 25 and 45.21 °C are shown by the blue hexagons (Carpenter and Jette, 1923), and between 10 and 25 °C by the blue open circles (Bonnell and Burrige, 1935). The epsomite–hexahydrate phase boundary, based on the compilation of Wagman et al. (1982) and DeKock (1986), is shown by the blue and red lines, respectively. Experimental results obtained in this study are shown by the large red circles along four humidity–buffer curves (near vertical gray lines), and the dashed line is the least-squares fit of the data. The equilibrium points for epsomite-saturated aqueous solutions are shown by the small solid triangles (Diesnis, 1935), the small dot (Archer and Rard, 1998), and small open triangles with apex pointing up, based on Pitzer’s model (Plummer et al., 1988). Those for the hexahydrate-saturated solutions reported by Carpenter and Jette (1923) are shown by the small blue open triangles with apex pointing down. The red open square is the invariant point for the assemblage EHAV predicted from our results at the invariant temperature of 48 °C (Linke and Seidell, 1965; horizontal solid line). (Modified from Fig. 1 of Chou and Seal, 2003a.)

Fig. 5). The open red square in Fig. 5 represents the invariant point A shown in Figs. 3 and 4 for the assemblage epsomite–hexahydrate–aqueous solution–vapor at well defined invariant T of 48 °C (Linke and Seidell, 1965). The black and blue dotted curves are the stability boundaries between epsomite and aqueous solution and between hexahydrate and aqueous solution, respectively. As shown in Fig. 5, it is apparent that (1) the epsomite–hexahydrate stability boundaries calculated from previously compiled thermodynamic data (Wagman et al., 1982; DeKock, 1986) are not reliable, because they did not intersect the invariant point A at 48 °C, and (2) the equilibrium reversal points of Chou and Seal (2003a) are in excellent agreement with previous vapor pressure measurements.

As reported by Chou and Seal (2003a), equilibrium constants and ΔG_r° values for reaction (4) were obtained from their experimental data using Eq. (5) and these values are listed in Tables 1 and 2, respectively. Fig. 7 shows the relation between $\ln K$ and $1/T$ for reaction (4); their reversal data can be represented by $\ln K$

Table 1
Derived equilibrium constants for reaction (4) at 0.1 MPa. (Table 2 of Chou and Seal, 2003a).

Humidity Buffer	T (°C) ^a	$f_{\text{H}_2\text{O}}$ (MPa) ^b	% RH ^c	$\ln K$
NaBr	28.01 ± 0.71	0.0037841	56.64 ± 0.38	-3.843 ± 0.038
KI	36.45 ± 0.31	0.0060957	66.71 ± 0.23	-3.202 ± 0.016
NaCl	42.25 ± 0.49	0.0083157	74.61 ± 0.13	-2.780 ± 0.026
KBr	44.18 ± 0.38	0.0091944	79.22 ± 0.26	-2.620 ± 0.020

^a Equilibrium T ; mean of the two values used to bracket equilibrium (see Table 1).

^b Calculated from Haar et al. (1984).

^c Calculated from Greenspan (1977).

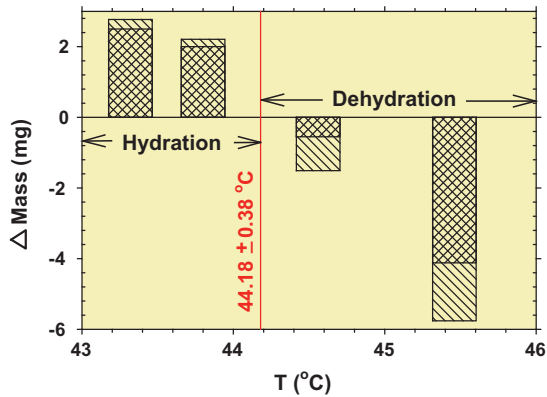


Fig. 6. Experimental results for reaction (4) along KBr buffer curve showing mass changes due to hydration at low temperatures and dehydration at high temperatures. Plotted are the data listed in Table 1 of Chou and Seal (2003a), and the reversal point is at 44.18 ± 0.38 °C (red circle on KBr buffer curve in Fig. 5). Results shown are for two separate samples at each temperature.

Table 2

Derived thermodynamic data for reaction (4) at 298.15 K and 0.1 MPa. (Table 3 of Chou and Seal, 2003a).

ΔG_r° (kJ mol ⁻¹)	ΔH_r° (kJ mol ⁻¹)	ΔS_r° (J mol ⁻¹ K ⁻¹)	Reference
10.13 ± 0.07	59.72 ± 0.76	166.3 ± 2.8	Chou and Seal (2003a)
10.11	59.11	164.3	Carpenter and Jette (1923)
10.22	65.18	184.3	Bonnell and Burridge (1935)
11.10 ± 1.4	59.91	163.7	Wagman et al. (1982)
10.89 ± 1.4	59.95	164.5	DeKock (1986)
10.21	-	-	Frowein (1887)
10.31	-	-	Lescoeur (1889)
10.35	-	-	Footo and Scholes (1911)
10.25	-	-	Bolte (1912)
10.15	-	-	Schumb (1923)

(± 0.012) = $20.001 - 7182.07/T$. The standard enthalpy of reaction, ΔH_r° , was calculated according to the relation:

$$\partial(\ln K)/\partial(1/T) = -\Delta H_r^\circ/R. \quad (6)$$

Values of ΔH_r° for reaction (4) are listed in Table 2. The entropy of reaction, ΔS_r° , was calculated from the relation:

$$\Delta G_r^\circ = \Delta H_r^\circ - T\Delta S_r^\circ, \quad (7)$$

and the obtained value is also listed in Table 2. These derived thermodynamic data were compared with previous data in Table 2.

The data of Chou and Seal (2003a) are in excellent agreement with all previous vapor pressure measurements, especially with those reported by Carpenter and Jette (1923), as shown in Table 2 and Figs. 5 and 7. The ΔG_r° value reported by Chou and Seal (2003a) is 1.0 and 0.8 kJ mol⁻¹ smaller than the value compiled by Wagman et al. (1982), and that compiled by DeKock (1986), respectively; it is still well within the ± 1.4 kJ mol⁻¹ uncertainty limits of Wagman et al. (1982) and DeKock (1986), but contains much smaller uncertainty (± 0.07 kJ mol⁻¹). Using these derived thermodynamic data, the epsomite–hexahydrate stability boundary can be extrapolated to other temperatures, as shown by the black dashed curve in Fig. 5. The validity of this phase boundary is further supported by the fact that it intersects the well-defined invariant point A (shown by the red open square in Fig. 5), where the coexisting aqueous phase is saturated with both epsomite and hexahydrate in the presence of a vapor phase at 0.1 MPa.

Similarly, the stability boundary between kieserite and hexahydrate needs to intersect the well-defined isobaric invariant point B

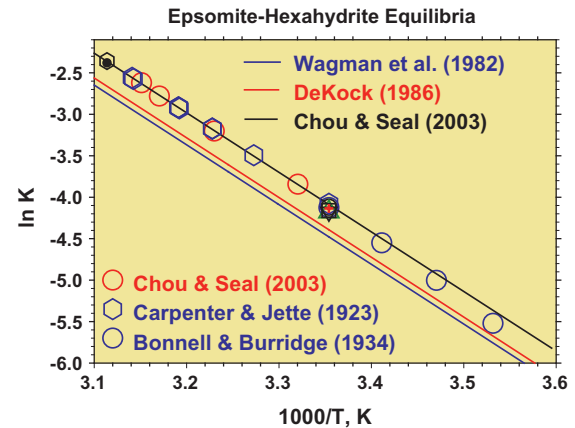


Fig. 7. Plot of $\ln K$ versus $1000/T$ for the epsomite–hexahydrate equilibria. Red circles are the data from Table 2, and the solid black line is a least-squares regression of those data. Previous data at 25 °C are shown by the large black open circle (Frowein, 1887), the black square (Lescoeur, 1889), the green triangle (Footo and Scholes, 1911), the red plus sign (Bolte, 1912), and the black triangle with apex pointing down (Schumb, 1923). The blue circles at 25 °C and lower temperatures are from Bonnell and Burridge (1935), and the blue hexagons at higher temperatures are from Carpenter and Jette (1923). The solid blue and red lines are based on the data compiled by Wagman et al. (1982) and DeKock (1986), respectively. The small black dot and hexagon at the upper left corner are the invariant point at 48 °C for the assemblage EHAV predicted from Pitzer's model (Plummer et al., 1988) for the epsomite-saturated solution and the data of Carpenter and Jette (1923) for the hexahydrate-saturated solution, respectively. (Modified from Fig. 2 of Chou and Seal, 2003a.)

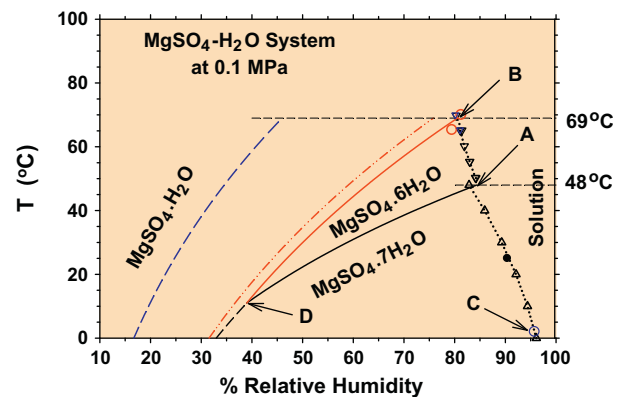


Fig. 8. Temperature–RH relations in the system $\text{MgSO}_4\text{--H}_2\text{O}$ at 0.1 MPa. The epsomite–hexahydrate curve (solid black line), the saturated aqueous solution curves (dotted curves connecting the open black triangles), small black dot, and the invariant point A are from Figs. 3–5. Curves calculated for the dehydration of hexahydrate to kieserite from the data of Wagman et al. (1982) (dashed blue curve) and from the data of DeKock (1986) (dash-dot-dot red curve) do not agree with the intersection of the hexahydrate-saturated solution boundary and the well-accepted temperature of the invariant assemblage hexahydrate–kieserite–aqueous solution–vapor of 69 °C (Linke and Seidell, 1965) (point B). The speculated position of the invariant point B (Chou and Seal, 2003a) is further confirmed by the positions of hexahydrate–kieserite coexisting points (two red circles) and the hexahydrate-saturated solutions (two small blue triangles) reported by van't Hoff et al. (1912). The hexahydrate–kieserite boundary was adjusted by drawing a curve (red solid) from the invariant point B parallel to the red dash-dot-dot curve of DeKock (1986), and this curve intersects the solid black curve at point D, which defines the invariant point for the assemblage epsomite–hexahydrate–kieserite–vapor at 11 °C and an RH of 39% and limits the lower stability of hexahydrate. The dashed black curve at lower temperatures is the speculated stability boundary between hexahydrate and kieserite. Note that the invariant point D can be at higher temperature and humidity if the solid red curve is parallel to the blue dashed curve of Wagman et al. (1982). The invariant point C (blue circle) locates at 2 °C and 95.8% RH for the assemblage meridianite–epsomite–aqueous solution–vapor, was used to evaluate low-temperature phase equilibria in Fig. 9.

shown in Fig. 8 at 69 °C for the assemblage kieserite–hexahydrate–aqueous solution–vapor, and can be approximated by drawing a curve (red line in Fig. 8) from point B parallel to the boundary curve (dashed-dot-dot red line in Fig. 8) derived from the data compiled by DeKock (1986), assuming her ΔH_r° value for the hexahydrate–kieserite dehydration reaction is correct. As reported by Chou and Seal (2003a) and shown in Fig. 8, this predicted kieserite–hexahydrate boundary curve intersects the epsomite–hexahydrate boundary curve at point D (at 11 °C), which defined another isobaric invariant point for the assemblage epsomite–hexahydrate–kieserite–vapor. Therefore, hexahydrate is not stable below 11 °C as shown in Figs. 3 and 8.

The humidity–buffer technique was applied by Chou and Seal (2007) to determine the stability boundary between hexahydrate ($\text{MgSO}_4 \cdot 6\text{H}_2\text{O}$) and starkeyite ($\text{MgSO}_4 \cdot 4\text{H}_2\text{O}$). They also used the derived thermodynamic data in the MgSO_4 – H_2O binary system to predict the stability of MgSO_4 minerals near the Martian surface (Fig. 9).

Recently, by using these thermodynamic data, their calorimetric data, and mathematical optimization technique, Grevel and Majzlan (2009) were able to provide an internally consistent thermodynamic data set for magnesium–sulfate hydrates, including standard entropy, standard enthalpy of formation, and standard Gibbs free energy of formation for epsomite, hexahydrate, starkeyite, and kieserite (see their Table 5).

4. Stability of sulfate and hydrated sulfate minerals of other metals

We demonstrated that the experimental reversal data for reaction (4), based on the humidity buffer technique, can be used to (a) define the equilibrium stability phase boundary between epsomite and hexahydrate, in the T – $\%RH$ space, with very small uncertainties, and (b) derive thermodynamic data for the minerals involved in the reaction.

Similarly, equilibrium constants for the reactions between melanterite ($\text{FeSO}_4 \cdot 7\text{H}_2\text{O}$) and rozenite ($\text{FeSO}_4 \cdot 4\text{H}_2\text{O}$) (Chou et al., 2002), chalcantite ($\text{CuSO}_4 \cdot 5\text{H}_2\text{O}$) and bonattite ($\text{CuSO}_4 \cdot 3\text{H}_2\text{O}$) (Chou et al., 2002), morenosite ($\text{NiSO}_4 \cdot 7\text{H}_2\text{O}$) and retgersite ($\text{NiSO}_4 \cdot 6\text{H}_2\text{O}$) (Chou and Seal, 2003b), $\text{CdSO}_4 \cdot 8/3\text{H}_2\text{O}$ and $\text{CdSO}_4 \cdot 5/3\text{H}_2\text{O}$ (Chou and Seal, 2004), goslarite ($\text{ZnSO}_4 \cdot 7\text{H}_2\text{O}$) and bianchite ($\text{ZnSO}_4 \cdot 6\text{H}_2\text{O}$) (Chou and Seal, 2005b), and bieberite ($\text{CoSO}_4 \cdot 7\text{H}_2\text{O}$)

and moorhouseite ($\text{CoSO}_4 \cdot 6\text{H}_2\text{O}$) (Chou and Seal, 2005a) were determined at temperatures between 25 and 98 °C and 0.1 MPa. High-quality thermodynamic data were derived from these reaction constants, including Gibbs free energy of reaction, enthalpy of reaction, and entropy of reaction.

Again, by using these thermodynamic data, their calorimetric data, and mathematical optimization technique, Grevel and Majzlan (2011) were able to provide an internally consistent thermodynamic data set for divalent metal–sulfate hydrates, including standard entropy, standard enthalpy of formation, and standard Gibbs free energy of formation for some metal sulfate hydrates containing Fe, Zn, Ni, Co, and Cu (see their Table 4). Recently, Kong et al. (2011a) extended the humidity–buffer technique to the study of the stability boundary between two trivalent ferric sulfates, kornelite ($\text{Fe}_2(\text{SO}_4)_3 \cdot 7\text{H}_2\text{O}$) and pentahydrate ($\text{Fe}_2(\text{SO}_4)_3 \cdot 5\text{H}_2\text{O}$), which is a stable phase but not a recognized mineral.

5. Terrestrial metal–sulfate efflorescent salts

Metal–sulfate salts play important roles in the cycling of metals and sulfate in terrestrial systems. They rarely occur in high temperature settings, found primarily in volcanic settings such as fumaroles. They are significantly more common in low temperature settings associated with the weathering of sulfide minerals. The mineral chemistry, phase equilibria, and paragenesis of metal–sulfate salts have been reviewed by Jambor et al. (2000). In this review, we will emphasize progress since this seminal contribution. In addition to Jambor et al. (2000), Hammarstrom et al. (2005) investigated secondary sulfate minerals at several sites in the eastern United States and included a review of many of the salient features of these compounds in the environment. Likewise, Jerz and Rimstidt (2003) considered paragenetic relationships among a variety of iron–sulfate minerals commonly found at abandoned mine sites, which, in part, built upon the work of Jambor et al. (2000).

5.1. High temperature settings

Sulfate minerals as a group are important minor constituents of high-temperature hydrothermal systems. Common hydrothermal sulfate minerals include barite, anhydrite, alunite, and jarosite. In fact, the presence of oxygen, sulfur, and hydrogen, in the case of alunite and jarosite, make these minerals invaluable tools for deciphering the hydrothermal history of mineral deposits through their stable isotope compositions (Rye, 2005). A review of these minerals is beyond the scope of this paper.

Simple metal–sulfate salts are rare in high temperature settings, presumably due to their generally high solubility especially at elevated temperatures. The only known occurrence of hydrothermal szomolnokite is found in the late stages of the Pascua high sulfidation epithermal Au–Ag–Cu deposit on the Chile–Argentina border (Chouinard et al., 2005). Szomolnokite is associated with pyrite in vuggy silica that post dated the main stages of Au–Ag–Cu mineralization. Chouinard et al. (2005) suggested that the szomolnokite formed between 80 and 220 °C on the basis of fluid-inclusion decrepitation data. The presence of szomolnokite is due, in part, to its retrograde solubility above 57 °C (Jambor et al., 2000).

Metal–sulfate salts are also found associated with volcanic fumaroles, crater lakes, and hot springs (Delines, 1975; Keith et al., 1981). In general, volcanic H_2S and SO_2 oxidize to form sulfuric acid, which reacts with the surrounding rocks to liberate metals, at which point, evaporation can lead to the formation of sulfate salts. Ferrous sulfate salts such as melanterite, rozenite, szomolnokite, the calcium sulfate gypsum, the aluminum sulfate

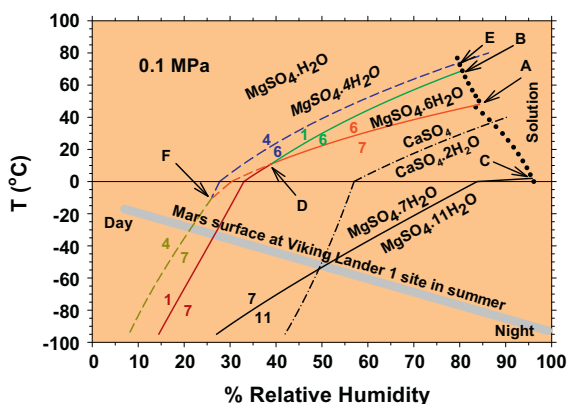


Fig. 9. Phase relations in the system MgSO_4 – H_2O at 0.1 MPa. Stable boundaries are shown by heavy solid curves, and metastable boundaries are shown by dashed curves. The invariant points from A to E and the saturated solution boundaries are from Figs. 3 and 8. Point F is another isobaric invariant point for the assemblage of epsomite–hexahydrate–starkeyite–vapor. Also shown is the stable boundary between gypsum ($\text{CaSO}_4 \cdot 2\text{H}_2\text{O}$) and anhydrite (CaSO_4), based on the data of Innorta et al. (1980) and DeKock (1986). Gray line indicates conditions at Viking Lander 1 site in summer (Savijärvi, 1995). (Modified from Fig. 6 of Chou and Seal, 2007.)

alunogen, and multicomponent salts such as halotrichite, tamarugite, voltaite, metavoltine, and copiapite are most common in these environments (Table 4).

5.2. Low temperature settings

5.2.1. Mineralogy

The sulfate salts in low-temperature environments are abundant; their number extends well beyond the simple sulfate salts that have thus far been investigated experimentally, as described above. To date, most experimental studies have been limited to simple salts with metal in a single valence state combined with sulfate and various numbers of water molecules. Examples include the $\text{Fe}^{2+}\text{SO}_4\text{-H}_2\text{O}$ and $\text{Cu}^{2+}\text{SO}_4\text{-H}_2\text{O}$ systems (Chou et al., 2002) and the $\text{Fe}_2^{3+}(\text{SO}_4)_3\text{-H}_2\text{O}$ system (Kong et al., 2011a). The plethora of mineral species results from the variety of ways of polymerizing sulfate tetrahedra (e.g., isolated tetrahedra, chains, sheets, and frameworks), the resulting variety of sites within the structures of these minerals with the ability to accommodate cations with different valences, and the occurrence of multiple mineral families

where the only chemical difference among the minerals is the number of hydration water molecules in the mineral formula (e.g., melanterite [$\text{Fe}^{2+}\text{SO}_4\cdot 7\text{H}_2\text{O}$], rozenite [$\text{Fe}^{2+}\text{SO}_4\cdot 4\text{H}_2\text{O}$], and szomolnokite [$\text{Fe}^{2+}\text{SO}_4\cdot \text{H}_2\text{O}$]) (Hawthorne et al., 2000). The mineral systems include simple monovalent salts such as mirabilite ($\text{Na}_2\text{SO}_4\cdot 10\text{H}_2\text{O}$), simple divalent salts such as gypsum ($\text{CaSO}_4\cdot 2\text{H}_2\text{O}$), simple trivalent salts such as coquimbite ($\text{Fe}_2^{3+}(\text{SO}_4)_3\cdot 9\text{H}_2\text{O}$), mixed valence salts such as halotrichite ($\text{Fe}^{2+}\text{Al}_2(\text{SO}_4)_4\cdot 22\text{H}_2\text{O}$; Fig. 10a), and hydroxysulfate minerals such as copiapite ($\text{Fe}^{2+}\text{Fe}_4^{3+}(\text{SO}_4)_6(\text{OH})_2\cdot 20\text{H}_2\text{O}$; Fig. 10b) or fibroferrite ($\text{Fe}^{3+}(\text{SO}_4)(\text{OH})\cdot 5\text{H}_2\text{O}$; Fig. 10c), all of which exhibit high solubility in water at ambient temperatures (Table 3). In natural assemblages, these phases are commonly associated with a variety of less soluble hydroxysulfate minerals such as jarosite ($(\text{K}, \text{Na}, \text{H}_3\text{O})\text{Fe}_3^{3+}(\text{SO}_4)_2(\text{OH})_6$), schwertmannite ($(\text{Fe}_8^{3+}\text{O}_8(\text{OH})_{8-2x}\cdot (\text{SO}_4)_x\cdot n\text{H}_2\text{O}$ where $1 \leq x \leq 1.75$, Bigham et al., 1996), alunite ($(\text{K}, \text{Na})\text{Al}_3(\text{SO}_4)_2(\text{OH})_6$), basaluminite ($\text{Al}_4(\text{SO}_4)(\text{OH})_{10}\cdot 4\text{H}_2\text{O}$), and aluminite ($\text{Al}_2(\text{SO}_4)(\text{OH})_4\cdot 7\text{H}_2\text{O}$, and ferric hydroxide minerals such as goethite (Fe^{3+}OOH) and ferrihydrite ($\text{Fe}^{3+}(\text{OH})_3$) (Bigham and Nordstrom, 2000).

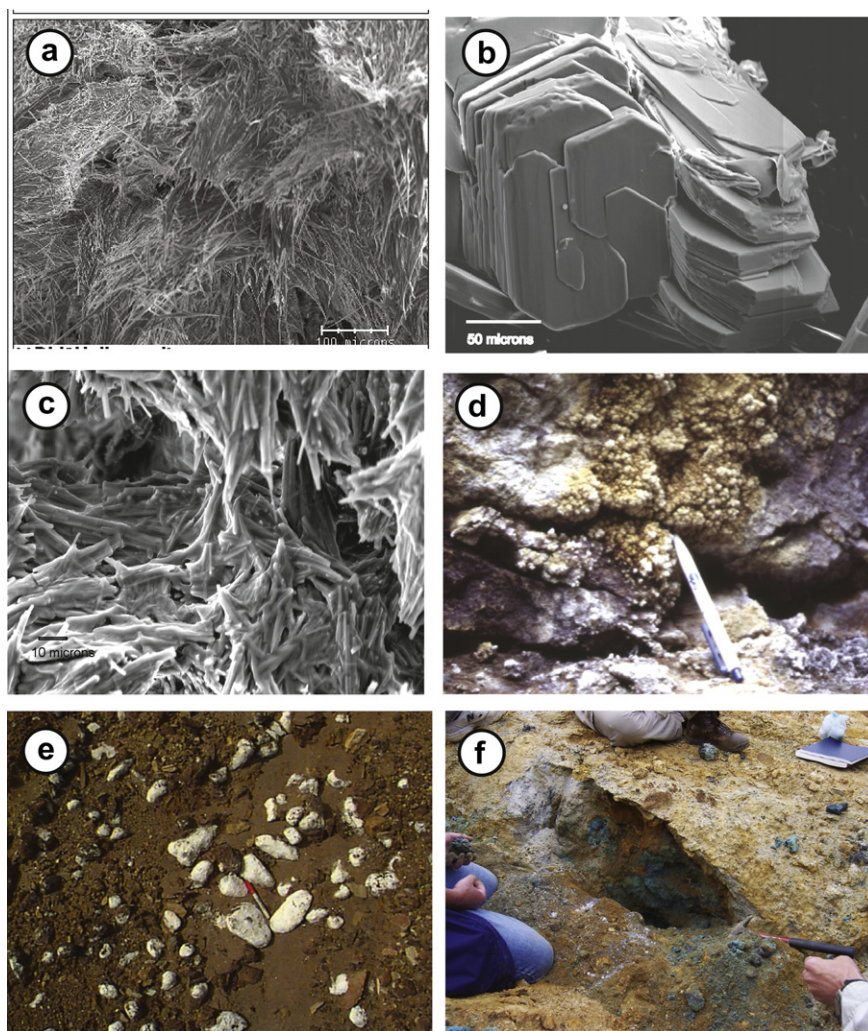


Fig. 10. Scanning electron microscopy (SEM) photomicrographs and photographs of metal-sulfate salts and associated phases. SEM photographs were taken by Jane Hammarstrom. (a) SEM photomicrograph of halotrichite “hair salts” from the Big Mike mine, Nevada; (b) SEM photomicrograph of copiapite from the Concepción mine, Spain; (c) SEM photomicrograph of fibroferrite from the Bumbarger–Iron King mine, Virginia; (d) Colliform, white gypsum “bloom” on the wall of the south pit at the Elizabeth mine, Vermont; (e) White rozenite crusts forming on pyrrhotite-rich waste-rock cobbles on historical waste-rock piles at the Elizabeth mine, Vermont. Brown material that the cobbles rest upon is composed of quartz, clays, sericite, ferric hydroxides and jarosite; (f) Blue, melanterite-rich evaporite layer below the surface of waste-rock piles (<0.5 m) at the Elizabeth mine, Vermont. The surrounding material is dominated by jarosite, quartz, and clays.

Table 3

Compilation of metal-sulfate salt occurrences associated with the weathering of sulfide minerals by geologic or mine waste setting. Sources: 1. Alpers et al. (1994), 2. Alpers et al. (2003), 3. Ávila et al. (2008), 4. Bauerek et al. (2009), 5. Bril et al. (2008), 6. Buckby et al. (2003), 7. Carmona et al. (2009), 8. Charles et al. (1986), 9. Cravotta (1994), 10. Delines (1975), 11. Dokoupilová et al. (2007), 12. Dold and Fontboté (2001), 13. Farkas et al. (2009), 14. Frondel and Palache (1949), 15. Gomes and Favas (2006), 16. Hammarstrom et al. (2005), 17. Jambor and Trill (1963), 18. Jerz and Rimstidt (2003), 19. Joeckel et al. (2005), 20. Keith et al. (1981), 21. Keith et al. (1999), 22. Khorasanipour et al. (2011), 23. Lottermoser (2005), 24. Martin et al. (1999), 25. Minakawa and Noto (1994), 26. Nordstrom and Alpers (1999), 27. Peterson and Wang (2006), 28. Piatak et al. (2004), 29. Rodgers et al. (2000), 30. Romero et al. (2006), 31. Sánchez España et al. (2005), 32. Seal et al. (2008), 33. Smuda et al. (2008), 34. Srebrodolskiy (1977), 35. Tuttle et al. (2009), 36. Valente and Leal Gomes (2008), 37. Whittig et al. (1982), 38. Yakhontova et al. (1988), 39. Zimbelman et al. (2005).

Mineral	Ideal formula	Active Volcanic Environment	Pyritic Shale	Coal Mine Waste	Volcanogenic Massive Sulfide Mine Waste	Porphyry Copper Mine Waste	Granite-related Sn-W Mine Waste	Mississippi Valley Type Mine Waste	Low-Sulfidation Epithermal Mine Waste	Magmatic Ni-Cu Mine Waste	Metallurgical Slag
Sources		8, 10, 20, 24, 25, 29, 34, 39	16, 17, 35, 37	9, 11	1, 2, 6, 16, 17, 18, 22, 26, 27, 30, 31, 32	12, 17, 22, 33	3, 15, 36	4	7, 13	14, 38	5, 23, 28
Monovalent											
Mirabilite	Na ₂ SO ₄ ·10H ₂ O	X	X			XX			X		
Thenardite	Na ₂ SO ₄	X	XX	X							
Divalent											
Melanterite	Fe ²⁺ SO ₄ ·7H ₂ O	XXX	XXX	XXX	XXX	XX	XXX	X			
Ferrohexahydrite	Fe ²⁺ SO ₄ ·6H ₂ O	X			X						
Siderotil	(Fe ²⁺ ,Cu)SO ₄ ·5H ₂ O	X			XX	X	XX				X
Rozenite	Fe ²⁺ SO ₄ ·4H ₂ O	XX	XX	XXX	XXX		XXX	X			
Szomolnokite	Fe ²⁺ SO ₄ ·H ₂ O	XX	XX	X	XX		XX				
Gypsum	CaSO ₄ ·2H ₂ O	XX	XXX	XXX	XXX	XX	XXX	X	X		XXX
Bassanite	CaSO ₄ ·0.5H ₂ O		XXX					X			X
Anhydrite	CaSO ₄	X		X							X
Epsomite	MgSO ₄ ·7H ₂ O		XX		XX			X	X		XX
Hexahydrite	MgSO ₄ ·6H ₂ O		XX	XX	XX	XX		X	X		XX
Pentahydrite	MgSO ₄ ·5H ₂ O		XX		X						
Starkeyite	MgSO ₄ ·4H ₂ O		XX		X		X		X		
Goslarite	ZnSO ₄ ·7H ₂ O				XX				X		
Bianchite	ZnSO ₄ ·6H ₂ O				X			X	X		X
Boyleite	ZnSO ₄ ·4H ₂ O							X			
Gunningite	ZnSO ₄ ·H ₂ O						X				
Chalcanthite	CuSO ₄ ·5H ₂ O	X			XXX	XX				X	X
Bonattite	CuSO ₄ ·3H ₂ O					XXX					
Mallardite	MnSO ₄ ·7H ₂ O				X		X				
Alpersite	(Mg, Cu)SO ₄ ·7H ₂ O				X						
Morenosite	NiSO ₄ ·7H ₂ O									XX	
Retgersite	NiSO ₄ ·6H ₂ O									XX	
Trivalent											
Quenstedtite	Fe ³⁺ (SO ₄) ₃ ·11H ₂ O	X									
Coquimbite	Fe ³⁺ (SO ₄) ₃ ·9H ₂ O			X	XX	XX			X		
Paracoquimbite	Fe ³⁺ (SO ₄) ₃ ·9H ₂ O				X						
Kornelite	Fe ³⁺ (SO ₄) ₃ ·7H ₂ O				X	XX					
Meta-alunogen	Al ₂ (SO ₄) ₃ ·27 H ₂ O	X	X				X				
Alunogen	Al ₂ (SO ₄) ₃ ·17 H ₂ O	XXX	XXX		XXX		XXX		X		
Mixed valence											
Romerite	Fe ²⁺ Fe ³⁺ (SO ₄) ₄ ·14H ₂ O	X		X	X						X
Bilinite	Fe ²⁺ Fe ³⁺ (SO ₄) ₄ ·22H ₂ O	X			X						
Halotrichite	Fe ²⁺ Al ₂ (SO ₄) ₄ ·22H ₂ O	XXX	XXX	XXX	XXX	XX	XX		X		
Pickeringite	MgAl ₂ (SO ₄) ₄ ·22H ₂ O		XXX	XXX	XX	XX	XX		X		
Apjohnite	MnAl ₂ (SO ₄) ₄ ·22H ₂ O		XX		X				X		
Dietrichite	ZnAl ₂ (SO ₄) ₄ ·22H ₂ O				X						
Potassium alum	KAl(SO ₄) ₂ ·12H ₂ O	X									
Tschermigite	NH ₄ Al(SO ₄) ₂ ·12H ₂ O	X	X								
Kalinite	KAl(SO ₄) ₂ ·11H ₂ O	X			X						

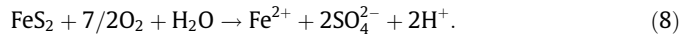
(continued on next page)

Table 3 (continued)

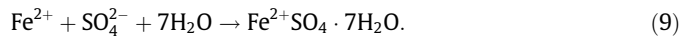
Mineral	Ideal formula	Active Volcanic Environment	Pyritic Shale	Coal Mine Waste	Volcanogenic Massive Sulfide		Porphyry Copper Mine Waste	Granite-related Sn–W Mine Waste	Mississippi Valley Type Mine Waste	Low-Sulfidation Epithermal Mine Waste	Magmatic Ni–Cu Mine Waste	Metallurgical Slag
					Mine Waste	Mine Waste						
Tamarugite	NaAl(SO ₄) ₂ ·6H ₂ O	XX	X					X				
Glauberite	CaNa ₂ (SO ₄) ₂	X										X
Blödite	Na ₂ Mg(SO ₄) ₂ ·4H ₂ O		XX				XX					
Picromerite	K ₂ Mg(SO ₄) ₂ ·6H ₂ O			X			X					
Syngenite	K ₂ Ca(SO ₄) ₂ ·H ₂ O			X						X		
Rhombochase	(H ₃ O)Fe ³⁺ (SO ₄) ₂ ·3H ₂ O			X		XX						
Voltaite	K ₂ Fe ²⁺ ·Fe ³⁺ (SO ₄) ₂ ·18H ₂ O	XX	X			XX				X		
Metavoltine	K ₂ Na ₆ Fe ²⁺ Fe ³⁺ (SO ₄) ₆ ·15H ₂ O	XX										
Hohmannite	Fe ³⁺ (SO ₄) ₂ ·8H ₂ O		XX									
Hydroxysulfates												
Copiapite	(Fe ²⁺ ·Fe ³⁺ (SO ₄) ₆ (OH) ₂ ·20H ₂ O	XX	XXX	XXX		XXX				XX		X
Aluminocopiapite	Al _{2/3} Fe ²⁺ (SO ₄) ₆ (OH) ₂ ·20H ₂ O		X			X			X			
Ferriccopiapite	Fe ²⁺ _{2/3} Fe ³⁺ _{4/3} (SO ₄) ₆ (OH) ₂ ·20H ₂ O		X			XX						
Magnesiocopiapite	MgFe ²⁺ _{4/3} (SO ₄) ₆ (OH) ₂ ·20H ₂ O		X			XX						
Fibroferrite	Fe ³⁺ (SO ₄) ₂ (OH)·5H ₂ O		X			X						
Botryogen	MgFe ³⁺ (SO ₄) ₂ (OH)·7H ₂ O		X			X						

5.2.2. Processes of formation

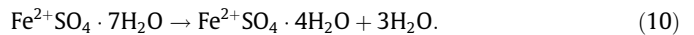
The oxidation of sulfide minerals, particularly pyrite, is a common process that initiates the formation of efflorescent metal–sulfate minerals. The oxidation of pyrite by molecular oxygen yields ferrous iron and sulfate (Rimstidt and Vaughan, 2003) as described by the reaction:



Upon desiccation, the ferrous iron and sulfate can combine to form melanterite through the reaction:



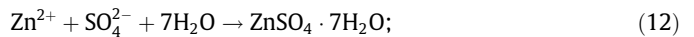
In natural systems, melanterite can easily dehydrate to form rozenite over the course of a day or less as described by the following reaction:



Likewise, the similar weathering reactions of sphalerite (ZnS) and chalcopyrite (CuFeS₂) can lead to the formation of goslarite (ZnSO₄·7H₂O) and chalcantite (CuSO₄·5H₂O), respectively, through the reactions:



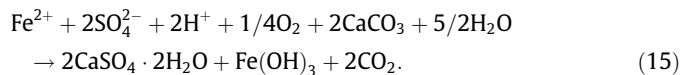
and,



and,



Copper can also occur in solid solution in melanterite rather than as its own discrete phase (Jambor et al., 2000). Metal–sulfate salts that contain non-sulfide components, like calcium in gypsum or aluminum in halotrichite, have a more complex paragenesis even though these two specific phases are as equally widespread as melanterite. For example, the acid generated from reaction (8) can then react with calcite in the rock. The reaction of acid with calcite results in neutralization of the acid, which can lead to the oxidation of the ferrous iron and its precipitation as ferric hydroxide as described by the mass-action reaction:



The precipitation of gypsum may occur at the site of calcite dissolution or may occur later in the flow path associated with evaporation. Gypsum blooms at abandoned mine sites that can be attributed to processes such as these are a common occurrence (Fig. 10d).

Similar reactions may be written for halotrichite where the aluminum is derived from feldspars, micas, clays or other silicate minerals. A prerequisite for these reactions is the generation of acid from pyrite or pyrrhotite oxidation, as shown above for gypsum formation, to enable the more refractory silicate minerals to be attacked. Furthermore, the low pH is also required to keep aluminum in solution for eventual precipitation along with ferrous iron and sulfate due to evaporation.

The formation of mixed valence iron sulfate salts or ferric iron salts requires a more complicated paragenesis. Jerz and Rimstidt (2003) considered the formation of sulfate, hydroxysulfates, and hydroxide phases in the system Fe–S–O–H in terms of neutralization, oxidation, and dehydration reactions. They found that in

specific systems, a trend characterized by these geochemical processes – oxidation, neutralization, and dehydration – explained the general sequence of phases found at several sites described in the literature. However, the details of individual sites are not as simple. Jambor et al. (2000) summarized paragenetic relationships from Iron Mountain, California (Nordstrom and Alpers, 1999), Alcaparrosa, Chile (Bandy, 1938), and a laboratory study (Buurman, 1975), which can be supplemented with observations by Jerz and Rimstidt (2003) from the Great Gossan Lead, Virginia. Even though the sequences of phases documented at these sites is unlikely to be due to a single, unidirectional geochemical and physical gradient, it is instructive to consider the phase transitions in terms of sequential reactions summarized in Tables 4 and 5. The assessment provided in Table 4 considers only sulfate phases in the system Fe–S–O–H and the reactions are written conserving iron in the solid phase. These studies also reported a number of phases outside of this system including halotrichite, pickeringite, and voltaite. All of the sequences begin with pyrite and commonly proceed through melanterite as an early hydrated ferrous sulfate,

which eventually dehydrates in a step-wise fashion to either rozenite, or more commonly szomolnokite before oxidation or sulfidation reactions commence. In addition, most of the sulfate minerals in the Fe–S–O–H system can contain impurities in solid solution that will expand their stability fields. In Table 5, the changes in geochemical conditions corresponding to each of these reactions are depicted in terms of species that are consumed or produced. This trend is opposite of the geochemical gradient needed to drive the reaction. For example, a reaction that consumes water will be favored by conditions of high activity of H₂O or high relative humidity. A more rigorous evaluation of geochemical changes associated with these reactions is precluded by the lack of thermodynamic data for many of these phases.

The paragenesis at Iron Mountain shows a consistent increase of the activity of H₂SO₄, or consumption of H₂SO₄, throughout the sequence (Nordstrom and Alpers, 1999). On an iron-conservative basis, the sequence includes both oxidation and reduction reactions. Similarly, the sequence also includes dehydration and hydration reactions and sulfidation or desulfidation reactions. Instead of

Table 4

Reactions among phases in the system Fe–S–O–H identified in the paragenesis of various sulfate deposits and in the laboratory resulting from pyrite oxidation.

<i>Iron Mountain (Nordstrom and Alpers, 1999)</i>	
Melanterite → Rozenite	
$\text{Fe}^{2+}\text{SO}_4 \cdot 7\text{H}_2\text{O} \rightarrow \text{Fe}^{2+}\text{SO}_4 \cdot 4\text{H}_2\text{O} + 3\text{H}_2\text{O}$	(IM1)
Rozenite → Szomolnokite	
$\text{Fe}^{2+}\text{SO}_4 \cdot 4\text{H}_2\text{O} \rightarrow \text{Fe}^{2+}\text{SO}_4 \cdot \text{H}_2\text{O} + 3\text{H}_2\text{O}$	(IM2)
Szomolnokite → Copiapite	
$5\text{Fe}^{2+}\text{SO}_4 \cdot \text{H}_2\text{O} + \text{H}_2\text{SO}_4 + \text{O}_2 + 15\text{H}_2\text{O} \rightarrow (\text{Fe}^{2+}\text{Fe}^{3+}(\text{SO}_4)_6(\text{OH})_2) \cdot 20\text{H}_2\text{O}$	(IM3)
Copiapite → Römerite	
$(\text{Fe}^{2+}\text{Fe}^{3+}(\text{SO}_4)_6(\text{OH})_2) \cdot 20\text{H}_2\text{O} + 2\text{H}_2\text{SO}_4 + 5\text{H}_2\text{O} \rightarrow 5\text{Fe}^{2+}\text{Fe}_2^{3+}(\text{SO}_4) \cdot 14\text{H}_2\text{O} + 1/2\text{O}_2$	(IM4)
Römerite → Coquimbite	
$2\text{Fe}^{2+}\text{Fe}_2^{3+}(\text{SO}_4) \cdot 14\text{H}_2\text{O} + \text{H}_2\text{SO}_4 + 1/2\text{O}_2 \rightarrow 3\text{Fe}_2^{3+} \cdot (\text{SO}_4)_3 \cdot 9\text{H}_2\text{O} + 2\text{H}_2\text{O}$	(IM5)
Coquimbite → Kornelite	
$\text{Fe}_2^{3+}(\text{SO}_4)_3 \cdot 9\text{H}_2\text{O} \rightarrow 3\text{Fe}_2^{3+}(\text{SO}_4)_3 \cdot 7\text{H}_2\text{O} + 2\text{H}_2\text{O}$	(IM6)
Kornelite → Rhomboclase	
$(\text{Fe}_2^{3+}(\text{SO}_4)_3 \cdot 7\text{H}_2\text{O} + \text{H}_2\text{SO}_4 + \text{H}_2\text{O} \rightarrow 2\text{H}_3\text{OFe}^{3+}(\text{SO}_4)_2 \cdot 3\text{H}_2\text{O}$	(IM7)
<i>Alcaparrosa (Bandy, 1938)</i>	
Szomolnokite → Römerite	
$3\text{Fe}^{2+}\text{SO}_4 \cdot \text{H}_2\text{O} + \text{H}_2(\text{SO}_4) + 10\text{H}_2\text{O} + 1/2\text{O}_2 \rightarrow \text{Fe}^{2+}\text{Fe}_2^{3+}(\text{SO}_4) \cdot 14\text{H}_2\text{O}$	(AL1)
Römerite → Quenstedtite	
$2\text{Fe}^{2+}\text{Fe}_2^{3+}(\text{SO}_4) \cdot 14\text{H}_2\text{O} + \text{H}_2(\text{SO}_4 + 2\text{H}_2\text{O} + 1/2\text{O}_2) \rightarrow 3\text{Fe}_2^{3+}(\text{SO}_4)_3 \cdot 10\text{H}_2\text{O}$	(AL2)
Quenstedtite → Coquimbite	
$\text{Fe}_2^{3+}(\text{SO}_4)_3 \cdot 10\text{H}_2\text{O} \rightarrow 3\text{Fe}_2^{3+}(\text{SO}_4)_3 \cdot 9\text{H}_2\text{O} + \text{H}_2\text{O}$	(AL3)
Coquimbite → Copiapite	
$5\text{Fe}_2^{3+}(\text{SO}_4)_3 \cdot 9\text{H}_2\text{O} \rightarrow 2(\text{Fe}^{2+}\text{Fe}_4^{3+}(\text{SO}_4)_6(\text{OH})_2) \cdot 20\text{H}_2\text{O} + 3\text{H}_2(\text{SO}_4 + 1/2\text{O}_2)$	(AL4)
Copiapite → Parabutlerite	
$(\text{Fe}^{2+}\text{Fe}_4^{3+}(\text{SO}_4)_6(\text{OH})_2) \cdot 20\text{H}_2\text{O} + 1/4\text{O}_2 \rightarrow 5\text{Fe}^{3+}(\text{SO}_4)(\text{OH}) \cdot 2\text{H}_2\text{O} + \text{H}_2\text{SO}_4 + 7/2\text{H}_2\text{O}$	(AL5)
<i>Great Gossan Lead (Jerz and Rimstidt, 2003)</i>	
Melanterite → Rozenite	
$\text{Fe}^{2+}\text{SO}_4 \cdot 7\text{H}_2\text{O} \rightarrow \text{Fe}^{2+}\text{SO}_4 \cdot 4\text{H}_2\text{O} + 3\text{H}_2\text{O}$	(GG1)
Rozenite → Copiapite	
$5\text{Fe}^{2+}\text{SO}_4 \cdot 4\text{H}_2\text{O} + \text{H}_2\text{SO}_4 + \text{O}_2 \rightarrow (\text{Fe}^{2+}\text{Fe}_4^{3+}(\text{SO}_4)_6(\text{OH})_2) \cdot 20\text{H}_2\text{O}$	(GG2)
Copiapite → Fibroferrite	
$(\text{Fe}^{2+}\text{Fe}_4^{3+}(\text{SO}_4)_6(\text{OH})_2) \cdot 20\text{H}_2\text{O} + 7/2\text{H}_2\text{O} + 1/4\text{O}_2 \rightarrow 5\text{Fe}^{3+}(\text{SO}_4)(\text{OH}) \cdot 5\text{H}_2\text{O} + \text{H}_2\text{SO}_4$	(GG3)
<i>Laboratory (Buurman, 1975)</i>	
Melanterite → Siderotil	
$\text{Fe}^{2+}\text{SO}_4 \cdot 7\text{H}_2\text{O} \rightarrow \text{Fe}^{2+}\text{SO}_4 \cdot 5\text{H}_2\text{O} + 2\text{H}_2\text{O}$	(LB1)
Siderotil → Rozenite	
$\text{Fe}^{2+}\text{SO}_4 \cdot 5\text{H}_2\text{O} \rightarrow \text{Fe}^{2+}\text{SO}_4 \cdot 4\text{H}_2\text{O} + \text{H}_2\text{O}$	(LB2)
Rozenite → Szomolnokite	
$\text{Fe}^{2+}\text{SO}_4 \cdot 4\text{H}_2\text{O} \rightarrow \text{Fe}^{2+}\text{SO}_4 \cdot \text{H}_2\text{O} + 3\text{H}_2\text{O}$	(LB3)
Szomolnokite → Rhomboclase	
$\text{Fe}^{2+}\text{SO}_4 \cdot \text{H}_2\text{O} + \text{H}_2\text{SO}_4 + 1/4\text{O}_2 + 2 1/2\text{H}_2\text{O} \rightarrow 2\text{H}_3\text{OFe}^{3+}(\text{SO}_4)_2 \cdot 3\text{H}_2\text{O}$	(LB4)
Rhomboclase → Coquimbite	
$2\text{H}_3\text{OFe}^{3+}(\text{SO}_4)_2 \cdot 3\text{H}_2\text{O} + \text{H}_2\text{O} \rightarrow \text{Fe}_2^{3+}(\text{SO}_4)_3 \cdot 9\text{H}_2\text{O} + \text{H}_2\text{SO}_4$	(LB5)
Copiapite → Römerite	
$(\text{Fe}^{2+}\text{Fe}_4^{3+}(\text{SO}_4)_6(\text{OH})_2) \cdot 20\text{H}_2\text{O} + 2\text{H}_2\text{SO}_4 + 5\text{H}_2\text{O} \rightarrow 5\text{Fe}^{2+}\text{Fe}_2^{3+}(\text{SO}_4) \cdot 14\text{H}_2\text{O} + 1/2\text{O}_2$	(LB6)

Table 5

Summary of geochemical changes associated with reactions presented in Table 4. Downward arrows indicate that the reaction consumes the component and upwards arrows indicate that the reaction produces the component. Dashes represent no change. Reaction numbers correspond to Table 4.

Reaction	Stage	H ₂ O	H ₂ SO ₄	O ₂
<i>Iron Mountain</i>				
IM1	Early	↑	–	–
IM2		↑	–	–
IM3	Late	↓	↓	↓
IM4		↓	↓	↓
IM5		↑	↓	↓
IM6		↑	–	–
IM7		↓	↓	–
<i>Alcaparrosa</i>				
AL1	Early	↓	↓	↓
AL2		↓	↓	↓
AL3	Late	↑	–	–
AL4		–	↑	↑
AL5		↑	↑	↓
<i>Great Gossan Lead</i>				
GG1	Early	↑	–	–
GG2		–	↓	↓
GG3	Late	↓	↑	↓
<i>Laboratory</i>				
LB1	Early	↑	–	–
LB2		↑	–	–
LB3	Late	↑	–	–
LB4		↓	↓	↓
LB5		↓	↑	–
LB6		↓	↑	↑

describing the salt-forming at Iron Mountain as a single flow path, Nordstrom and Alpers (1999) described it in terms of three general end members: settings closely associated with pyrite, higher flow settings, and stagnant “dead ends” within the mine workings. The pyritic and higher flow settings are dominated by ferrous sulfate minerals due to the strong reducing capacity of pyrite, the slow rates of iron oxidation, and low *pH*. The stagnant parts of the mine workings allow more time for iron oxidation.

At Alcaparrosa, Chile, the paragenesis is equally complex (Bandy, 1938; Table 4), suggesting an equally complex association of geochemical environments. In contrast, the shorter sequence described by Jerz and Rimstidt (2003) at the Bumbarger–Iron King mine in the Great Gossan Lead in southwestern Virginia is somewhat simpler. Most of the sequence can be considered in terms of increasing amounts of oxidation, dehydration, and sulfidation. The study of Buurman (1975) is a little more perplexing because the experiment took leachate from a pyrite concretion and allowed it to dry under laboratory conditions, without specific details of the laboratory conditions such as prevailing temperature or relative humidity provided. The sequence exhibits progressive consumption of water, but oxidation–reduction, and sulfidation–desulfidation steps are not consistent.

The beginning and end of the sequences at Alcaparrosa and the Great Gossan Lead provide an interesting comparison (Table 4). They each begin with chemically similar phases except for the number of waters of hydration (szomolnokite Fe²⁺SO₄·H₂O versus rozenite Fe²⁺SO₄·4H₂O, respectively), and end with chemically similar phases except for the number of waters of hydration (parabulterite Fe³⁺(SO₄)(OH)·2H₂O versus fibroferrite Fe³⁺(SO₄)(OH)·5H₂O, respectively). This difference in hydration state between the two sites may reflect differences in the ambient humidity at the sample site, or the differences in the ambient humidity at the site where the mineralogical identification were done and the challenges of preserving unstable mineral species in the field for later mineralogical characterization. A major source of ambiguity in interpreting

natural assemblages is the challenge of collecting sampling, returning them to the laboratory, and analyzing them by various techniques without alternating the mineralogy. Hydrated sulfate minerals are known to react rapidly in terms of hydration and dehydration reactions, and also oxidation reactions for those containing ferrous iron, such that the mineralogy at the time of collection may be different from that analyzed in the laboratory (Zodrow et al., 1979; Chou et al., 2002; Hyde et al., 2011).

5.2.3. Occurrences

Efflorescent metal–sulfate salts are commonly found associated with sulfide minerals from a variety of low-temperature geologic settings. Settings include sulfidic shales, coal beds and their mine wastes, a variety of mineral deposit types and their mine wastes, and pyrometallurgical slag. Due to the high solubility of most of these phases, they are most common in settings that have a limited or ephemeral supply of water. These environments include settings in arid climates or seasonally dry climates, protected areas in mine workings, within the vadose zone of mine-waste piles, or under overhangs such as cliffs or road cuts.

Table 3 summarizes metal–sulfate mineral occurrences from the geologic settings listed above. This compilation emphasizes data from studies published since Jambor et al. (2000), but does include results from that paper and papers cited by that study, particularly for settings that have received limited attention in the literature since then. Table 3 provides a qualitative assessment of the abundance of these minerals based on the frequency of their identification rather than an estimate of their modal abundance in the field. However, for settings for which only a single report was found, qualitative information about the relative abundance of the phases was used to rank their importance. The table is dominated by sulfate salts where one or more cations combine with sulfate, with or without water molecules. Selected hydrated hydroxysulfate minerals such as copiapite are included in the table because they are commonly associated with the metal–sulfate salts and exhibit similar solubility and geochemical behavior in the environment.

One of the most striking features of Table 3 is the overall abundance of iron-bearing sulfate salts. This abundance is a reflection of the fact that the weathering of pyrite or pyrrhotite is the ultimate source for many of these phases. The near ubiquity of sulfates such as gypsum, halotrichite, and alunogen in these sulfate–mineral assemblages attests to the importance of the acid generated from pyrite or pyrrhotite oxidation in attacking and solubilizing elements like calcium and aluminum from silicate minerals in the vicinity of the iron-sulfide minerals. The overall frequency of occurrence of simple salts presented in Table 3 matches well with their stabilities in Fig. 11. Melanterite and rozenite are the most common ferrous sulfates found at most sites; the dehydration reaction relating these two phases lies near the middle of the range of eastern United States summer temperature and humidity. Likewise, epsomite and hexahydrate are the most commonly identified magnesium sulfates, which also is consistent with the central location of the dehydration reaction relating these minerals. The zinc sulfates goslarite and bianchite are far more common than gunningite, which is stable at lower humidity than the more common phases. Finally, the dominant cupric sulfate is chalcantite, which has a wide stability field spanning most common temperature and humidity conditions.

Another interesting feature of Table 3 is the distribution of base-metal (Cu and Zn) sulfates minerals such as chalcantite, bonattite, alpersite, goslarite, bianchite, boyleite, gunningite, die-trichite, mallardite, and apjohnite. The systems, such as active volcanic environments, pyritic shales, and coal deposits, that lack base-metal sulfide minerals tend not to have these minerals. They are almost invariably associated with base and precious metal

fine-grained oxidized waste material dominated by jarosite, mixed with cobbles of subeconomic ores, dominated by pyrrhotite with lesser amounts of chalcopyrite and sphalerite. During the course of day, white coatings were commonly observed forming on the surface of the cobbles (Fig. 10e). The white coatings were mostly rozenite. Melanterite was also common as were halotrichite-pickeringite, chalcantite, copiapite, and fibroferrite; jarosite, schwertmannite, and gypsum were ubiquitous (Hammarstrom et al., 2005). During rain events, the rozenite would dissolve. Some of the drainage would leave the piles as sheet flow, producing effects in Copperas Brook similar to those documented by Dagenhart (1980). Some of the drainage would infiltrate the pile, forming buried evaporite layers, typically dominated by melanterite (Fig. 10f). The presence of melanterite in the subsurface rather than rozenite reflects the higher humidity found in the vadose zone of the waste-rock piles. Blowes et al. (1991) found similar accumulations of melanterite in the subsurface of tailings piles at the Heath Steele mine, New Brunswick, Canada. The evaporite layers generally do not get significantly wetted during rain storms, and continue to accumulate through much of the year. However, during spring melting of the winter snow pack, the piles reach saturation, the evaporite layers become wet, and the efflorescent salts dissolve. This dissolution is reflected in the peak sulfate loads seen in Copperas Brook draining the area during the spring (Fig. 13). Peak copper loads in Copperas Brook also correspond to this seasonal flushing event.

Ferrous iron-sulfate minerals can contain significant concentrations of other divalent metals in solid solution. Melanterite can contain a number of other metals in solid solution beyond ferrous iron. The review by Jambor et al. (2000) found that the $\text{CuSO}_4 \cdot 7\text{H}_2\text{O}$ and $\text{ZnSO}_4 \cdot 7\text{H}_2\text{O}$ components can substitute up to 50 mol% into the melanterite lattice – the maximum amount possible to retain that mineral designation. Further, siderotil, nominally $\text{Fe}^{2+}\text{SO}_4 \cdot 5\text{H}_2\text{O}$, is unstable in the $\text{Fe}^{2+}\text{SO}_4\text{-H}_2\text{O}$ system relative to melanterite and rozenite, and instead requires a minimum of 5 mol% Cu to stabilize it (Jambor and Traill, 1963). In contrast, Hammarstrom et al. (2005) found less than 5 mol% of Cu, Zn, and Mn substituting into halotrichite associated with mine waste from abandoned polymetallic massive sulfide deposits. However, they did identify the Zn–Mn end-member solid solution, dietrichite-apjohnite. Similarly, Jamieson et al. (2005) found less than 5 mol% substitution of Cu and Zn

for Fe^{2+} and Mg in copiapite-group minerals from Iron Mountain, California. Thus, dissolution of ferrous iron sulfate salts can release significant quantities of other trace metals that may have greater environmental consequences than the iron that is present in greater abundance.

6. Stability field, phase transition pathways, and reaction rates of hydrous sulfates under the conditions relevant to Mars

6.1. Occurrence of Martian sulfates

Recent findings of Mg, Ca and Fe sulfates on Mars have reinforced the importance of sulfates in Martian geology, as indicators of past geologic environments, potential hosts for water, and acid sinks. Sulfur cycling, sulfur redox state changes during sulfur cycling, and the effects of S-bearing species as alteration agents for surface and subsurface materials are all important factors in the hydrological and chemical evolution of the Martian surface through time.

Among the Martian sulfates, Ca and Mg sulfates were observed by orbital remote sensing (by OMEGA instrument on Mars Express and CRISM instrument on Mars Reconnaissance Orbiter, MRO) showing wide distributions and large quantities. Many of these sulfates, especially polyhydrated sulfates, occur in layers that have the thicknesses rarely seen in terrestrial deposits, e.g., 200–400 m thick at Aram Chaos, ~2 km thick at Gale Crater (where Mars Science Laboratory rover, MSL, has landed) and ~400 m thick at Capri Chasma (Lichtenberg et al., 2009; Milliken et al., 2009; Roach et al., 2009, 2010a, 2010b). The mineralogical details of these thick deposits are worthy of in-depth investigations in current (Opportunity and MSL rovers) and future landed missions (MSL and ExoMars). Furthermore, the environmental conditions that enabled such large amount of layered sulfate deposition need to be investigated.

Compared with Mg- and Ca-sulfates, orbital remote sensing detected Fe sulfates only in localized areas (Lichtenberg et al., 2010; Roach et al., 2010b; Milliken and Bish, 2010). Nevertheless, Fe sulfates were identified with more mineralogical detail during the Mars Exploration Rover (MER) missions. Among them, jarosite was identified in Meridiani outcrop (Klingelhofer et al., 2004), and a variety of ferric sulfates were found in subsurface salty soils at Gusev (Morris et al., 2006, 2008; Gellert et al., 2006; Lane et al., 2008; Ming et al., 2008; Johnson et al., 2007; Wang et al., 2008). More importantly, the dehydration of ferric sulfates was implied on the basis of a set of Pancam observations that revealed a temporal color change of the subsurface salty soils from tens of centimeters depth at Tyrone site (near Home Plate, at Gusev) after being excavated and exposed to the Martian surface atmospheric conditions (Wang et al., 2008; Wang and Ling, 2011).

Hydrated sulfates were discovered in Martian meteorites, such as sulfates in Martian SNC meteorite such as Nakhla, QUE94201, Shergotty, Chassigny, and ALH84001 (Wentworth and Gooding, 1993, 1994, 1996; Wentworth et al., 2000, 2002), and jarosite and Ca-sulfates in meteorite MIL03346 (McCubbin et al., 2009; Herd, 2006; Vicenzi et al., 2007).

The types of hydrous sulfates that we currently see on Mars depend on many factors that include precipitation conditions (brine chemistry, T , pH , Eh , RH); the stability field of individual sulfates during Mars climatic variation (the obliquity changes, seasonal and diurnal cycles); and the reaction rates of phase changes. Because of the slow kinetics of many reactions in the current low temperature conditions at Martian surface and subsurface, metastable phases will be observed from non-equilibrium processes, which place a high priority on the study of phase transitions pathways of hydrous sulfates.

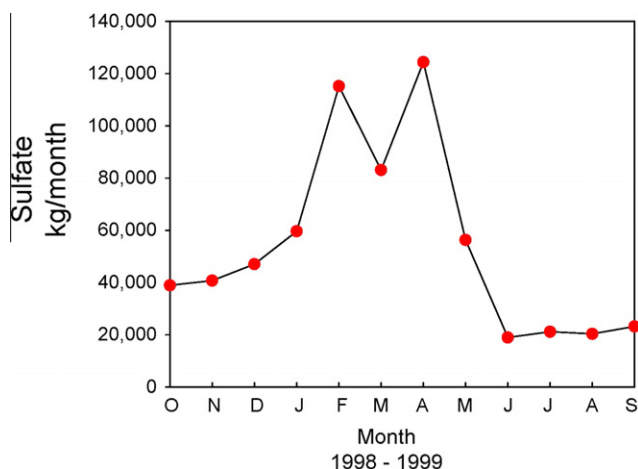


Fig. 13. Monthly variation of the sulfate load in Copperas Brook, which drains the Elizabeth Copper Mine Superfund site, Vermont from October 1998 to September 1999. The peak sulfate load in the Spring months reflects the saturation of the waste piles due to melting of the winter-long snow pack, and the dissolution of melanterite-rich evaporite layers at depth (Fig. 10f). Typical summer rain events are insufficient to saturate the waste piles. Instead, infiltration of rain and subsequent evaporate serves to build these evaporate layers.

6.2. Experiments on the stability field, phase transition pathways, and reaction rates of Mg-sulfates

6.2.1. Experiments in three stages

We have conducted a systematic experimental study of hydrated Mg sulfates. This study consisted of three stages. First, eleven distinct Mg-sulfates, anhydrous and hydrous, crystalline and non-crystalline, were synthesized, with their structures confirmed by X-ray diffraction, and the standard Raman, Vis-NIR (0.4–2.5 μm), and MIR (2.5–25 μm) spectra taken on the same samples (Wang et al., 2006). The unique Raman spectra of these sulfates obtained in this phase were used for non-invasive phase identification of the intermediate reaction products in second stage experiments.

In the second stage (Wang et al., 2009), 173 experiments were conducted to study the stability field and phase transition pathways of six Mg sulfates. These experiments included anhydrous MgSO_4 (0w) at 50 °C in 5–100% RH range; epsomite $\text{MgSO}_4 \cdot 7\text{H}_2\text{O}$ (7w), starkeyite $\text{MgSO}_4 \cdot 4\text{H}_2\text{O}$ (4w), monohydrate $\text{MgSO}_4 \cdot \text{H}_2\text{O}$ (1w), and amorphous $\text{MgSO}_4 \cdot 2\text{H}_2\text{O}$ (Am) at three temperatures

50 °C, 21 °C, 5 °C, and 10 RH levels from 6% to 100%; meridiannite $\text{MgSO}_4 \cdot 11\text{H}_2\text{O}$ (11w), epsomite $\text{MgSO}_4 \cdot 7\text{H}_2\text{O}$ (7w), starkeyite $\text{MgSO}_4 \cdot 4\text{H}_2\text{O}$ (4w), monohydrate $\text{MgSO}_4 \cdot \text{H}_2\text{O}$ (1w), and amorphous $\text{MgSO}_4 \cdot 2\text{H}_2\text{O}$ (Am) at –10 °C and six RH level from 11% to 97%; and mixtures of epsomite (7w) with Ca and Fe sulfates and Fe hydroxide and oxide at selected T and RH. The purpose of experiments on mixtures was to study the catalytic effect of these Ca- and Fe-bearing phases (often precipitated in nature with Mg sulfates) on the dehydration of epsomite. The T and RH conditions were selected on the basis of the experiments of pure Mg sulfates.

In the third stage (Wang et al., 2011), we extracted the reaction rate information based on the timing of phase conversion occurred during the second stage for five important processes of dehydration and rehydration. The main purpose of our study was to understand Mg-sulfate occurrence on Mars, on which the observed surface-temperature range in the equatorial region was about 294–180 K (Smith et al., 2004, 2006; Spanovich et al., 2006). Therefore for the high T limit in experiments, we selected 50 °C based on a general understanding that was the upper limit T in the history of Mars (except in the extreme cases of volcanic, impact, and during

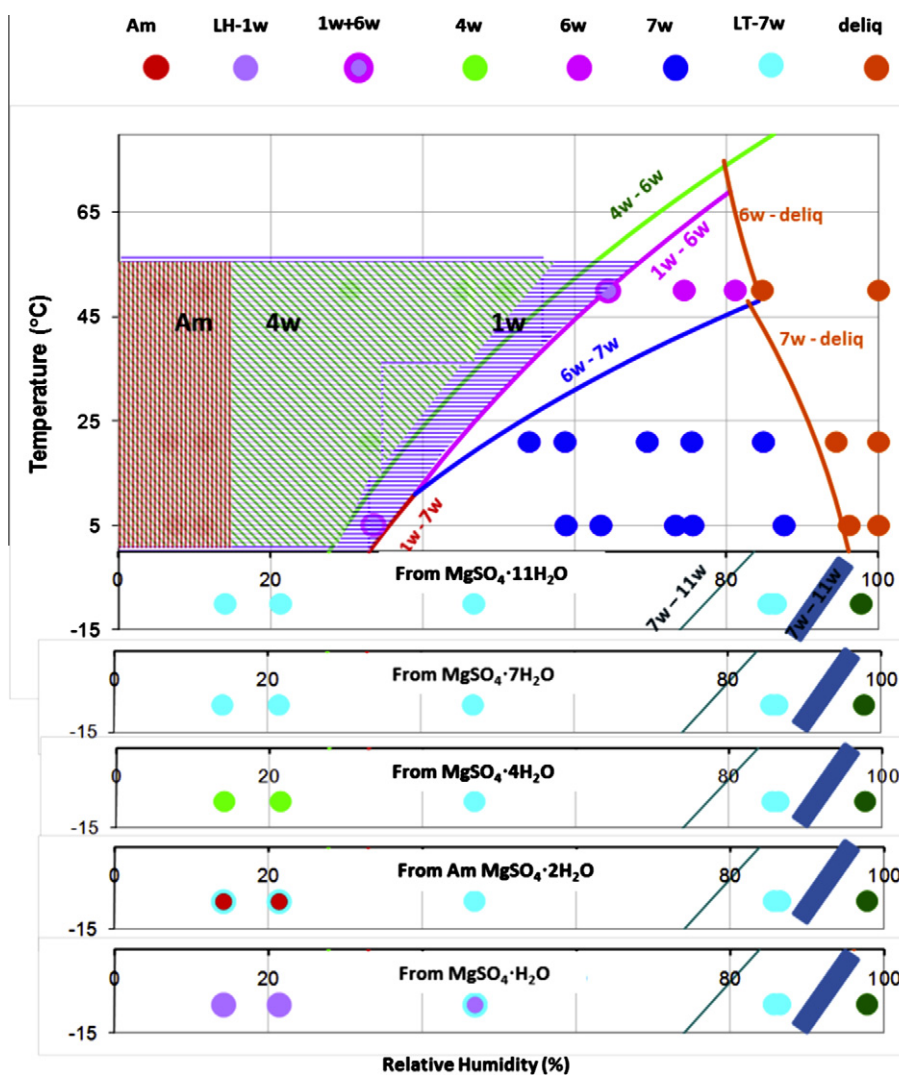


Fig. 14. The final phases of Mg-sulfates from 150 experiments on the stability and phase transition pathways (ten RH levels at 50 °C, 21 °C, and 5 °C [see Table 2 of Wang et al. (2009)], and six RH levels at –10 °C [see Table 2 of Wang et al. (2011)]). The phase identifications (annotated by colored circles, where observed mixed phases are presented as one color in center circled by second color) were made on the basis of their Raman spectra. The phase boundaries (as thin lines) of 4w–6w, 1w–6w, 6w–7w, 1w–7w, 6w–deliq, 7w–deliq, and 7w–11w are from Chou and Seal (2003a, 2007). The shadowed areas above 0 °C (marked as Am, 4w, and 1w) indicate the overlaps of stability/metastability fields of these three phases. Below 0 °C, each row corresponds to a different starting phase (marked in that row). The location of actual 7w–11w phase boundary (shown as a wide zone in each of five rows below 0 °C) is based on the experimental observations. Modified from Fig. 1 of Wang et al. (2011).

hydrothermal event). To run a laboratory dehydration/rehydration experiment at $-100\text{ }^{\circ}\text{C}$ would require unrealistically long durations to observe any phase change, thus we selected $-10\text{ }^{\circ}\text{C}$ as the lower T limit but used an extrapolation to estimate the reaction rate at low temperature extremes on Mars.

6.2.2. Results and discussions

6.2.2.1. Stability fields and phase transition pathways of common Mg-sulfate hydrates. The final phases of Mg sulfates from 120 experiments at $50\text{ }^{\circ}\text{C}$, $21\text{ }^{\circ}\text{C}$, $5\text{ }^{\circ}\text{C}$ and ten RH levels are shown as colored data points in the upper part of Fig. 14. The final phases of 30 experiments at $-10\text{ }^{\circ}\text{C}$ are shown in five rows of data points below $0\text{ }^{\circ}\text{C}$ (Fig. 14), with each row corresponding to a different starting phase (marked in that row). The phase identifications (annotated by colored circles) were made on the basis of their Raman spectra. The phase boundaries of 4w–6w, 1w–6w, 6w–7w, 1w–7w, 6w–deliq, 7w–deliq, and 7w–11w are from Chou and Seal (2003a, 2007). The shaded areas above $0\text{ }^{\circ}\text{C}$ (marked as Am, 4w, and 1w) indicate the overlaps of stability/metastability fields of these three phases.

The stability/metastability fields of 7w, 6w, 4w, 1w observed in our experiments are consistent with the above phase boundaries. However, the stability field of 11w is inconsistent with the prediction of Chou and Seal (2007). In our experiments, all five starting phases converted to LT-7w (a $\text{MgSO}_4 \cdot 7\text{H}_2\text{O}$ with a structure distorted from epsomite) at $-10\text{ }^{\circ}\text{C}$ and a RH value buffered by NaCl-saturated aqueous solution, indicating that 11w–7w phase boundary passes a point in the RH zone (Fig. 14) defined by the NaCl- and KCl-saturated aqueous solutions on each side at $-10\text{ }^{\circ}\text{C}$, i.e., the stability field of meridianiite ($\text{MgSO}_4 \cdot 11\text{H}_2\text{O}$) at $-10\text{ }^{\circ}\text{C}$ is limited in a much narrow RH range ($>88\%$) than 77.24% as predicted by Chou and Seal (2007). This discrepancy can be caused by the uncertainty associated with the position of the isobaric invariant point at $2\text{ }^{\circ}\text{C}$ and 95.77% RH for the coexistence of 7w, 11w, aqueous phase, and a vapor phase used by Chou and Seal (2007) to make their prediction.

Fig. 15 shows the pathways of Mg-sulfate phase transitions at Martian T and RH conditions, based on our experiments. Notice in these experiments, we observed two special pathways for the dehydration of epsomite (7w). The normal product from the dehydration of epsomite on Mars should be starkeyite (4w, Fig. 15). The energy barrier placed by ordinary Martian surface temperatures (past and present) would prevent direct dehydration from epsomite (7w) to monohydrate. Moreover, starkeyite has a broad stability/metastability field (Fig. 14) in mid-low temperature conditions and low relative humidity (-10 to $50\text{ }^{\circ}\text{C}$ and $6\text{--}34\%$ RH in our experiments) (Chou and Seal, 2007; Chipera and

Vaniman, 2007; Wang et al., 2009). Starkeyite is one of the candidates for polyhydrated sulfates found on Mars with wide occurrences, based on its similar NIR spectral pattern to those observed by orbital remote sensing on Mars.

The dehydration of epsomite (7w) can progress to the monohydrate stage on Mars under two circumstances (Fig. 15), as follows: (1) a monohydrate Mg-sulfate formed at low RH (LH-1w, details to be discussed in 6.2.2.2.) could form at locations where the chemistry of the original brine allowed the co-precipitation of Ca sulfates and Fe sulfates or allowed the coexistence of Mg sulfates with other minerals (including Fe oxides). Our experiments (Wang et al., 2009) suggest that some coexisting species would function as a catalyst in the dehydration process of epsomite to help overcome the kinetic barrier and to reach the monohydrate stage (LH-1w in Fig. 15); (2) at locations where amorphous Mg sulfates first formed by rapid dehydration of epsomite, a continuous reduction of $f(\text{H}_2\text{O})$ could further drive the dehydration of the amorphous Mg-sulfate phase (with irregular and less-stable structure) to the monohydrate stage (LH-7w in Fig. 15, Wang et al., 2006, 2009).

6.2.2.2. New phases of Mg-sulfate hydrates and their anticipated occurrence on Mars. During the study of stability field and phase-transition pathways, we found two new phases in the series of Mg-sulfate hydrates; a $\text{MgSO}_4 \cdot \text{H}_2\text{O}$ (abbreviated as LH-1w) phase with a different structure from kieserite (abbreviated as MH-1w), and a $\text{MgSO}_4 \cdot 7\text{H}_2\text{O}$ (abbreviated as LT-7w) phase with a distorted structure from epsomite (abbreviated as RT-7w). Both new phases play important roles in the pathways of the phase transitions among other hydrous Mg-sulfates.

We note that the LH-1w is the end product of dehydration reactions from all Mg sulfates with the hydration degree greater than one (Wang et al., 2009), and this phase is very stable in the T - RH range relevant to Martian surface conditions (Chipera and Vaniman, 2007; Wang et al., 2009). Therefore, this phase should be observed on Mars as widespread dehydrated Mg sulfate. The LH-1w has a distinctive Raman spectrum (Fig. 16) and XRD pattern relative to those of kieserite (MH-1w). Its VIS–NIR reflectance spectral

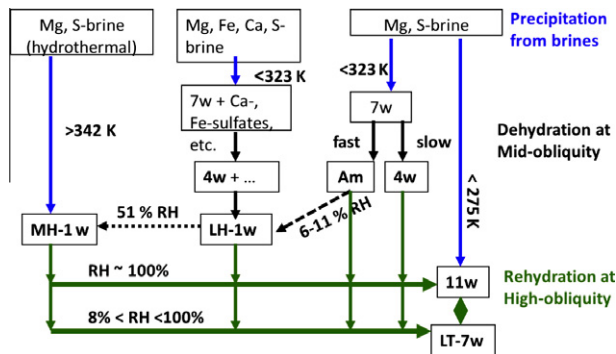


Fig. 15. Precipitations and phase transition pathways of Mg-sulfates on Mars, based on experiments (Wang et al., 2006, 2009, 2011). Blue arrows mark the precipitations, black arrows mark the dehydration at mid-obliquity period, and green arrows mark the rehydration/dehydration at high-obliquity period. Modified from Fig. 12 of Wang et al. (2011).

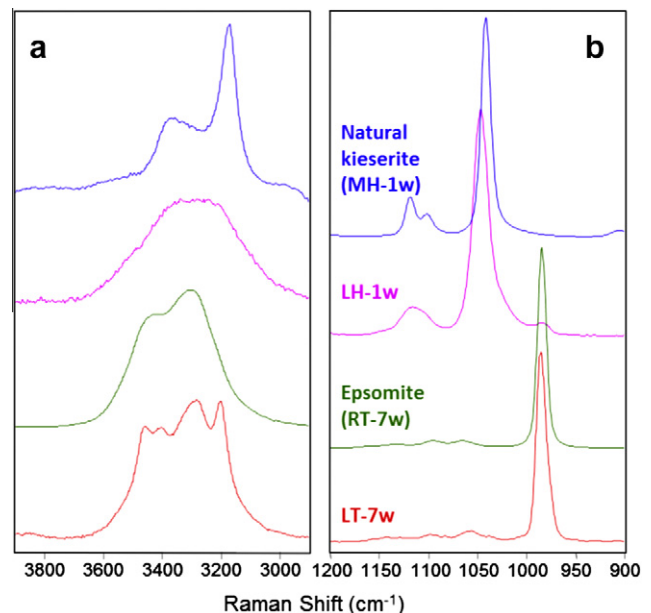


Fig. 16. Distinct Raman spectra of natural kieserite (MH-1w) and LH-1w, epsomite (RT-7w) and LT-7w. (a) Spectral region for H_2O vibrational modes; (b) Spectral region for symmetric stretching vibrational mode of $[\text{SO}_4]^{2-}$ tetrahedra.

pattern is similar to that of kieserite, with slightly different spectral details (Fig. 17). Because of the generally low signal-to-noise ratio (S/N) in the spectra of Martian sulfates obtained from orbital remote sensing spectrometers (OMEGA and CRISM), the distinction of LH-1w from MH-1w on Mars has not been achieved yet. On the basis of the study of its stability field, phase boundaries relative to other phases, and probable phase transition pathways, the widely observed “kieserite” spectral feature on Mars is most likely the result of widespread presence of LH-1w.

LH-1w can convert to the kieserite (MH-1w), but only under a higher RH and at moderate temperature (at 51% RH and 50 °C in our experiments, shown as dotted line in Fig. 15 from Wang et al., 2009). In other words, the likelihood of this conversion is very low under current ordinary Martian surface conditions. Based on phase relations (Chou and Seal, 2003a), kieserite (MH-1w) would precipitate from Mg-S-H₂O brine at $T > 69$ °C, thus the probability of kieserite occurrence during localized hydrothermal events (or other high T events such as volcanic and impact) on Mars does exist (Fig. 15).

A MgSO₄·7H₂O (LT-7w) phase with a distorted structure from epsomite was observed as the dehydration product of 11w at -10 °C and RH < 88%, and rehydration products from 1w, 4w, Am (2w) at -10 °C and RH > 11%. Fig. 14 shows a stability field of this phase with wide RH range at -10 °C; we would anticipate an even wider stability field at much lower T.

A wide stability field of LT-7w is an important factor to understand the current Mg-sulfate species on Mars, especially for subsurface and polar regions. For example, during the seasonal change in Martian polar regions when water ice sublimates, the coexisting meridianiite (MgSO₄·11H₂O) should convert to LT-7w in a wide RH range, as indicated in our experiments (Wang et al., 2011), such that LT-7w would be one of the two most common hydrated Mg sulfates (meridianiite would be another) at temperatures ≤ -10 °C on Mars, including subsurface and polar settings.

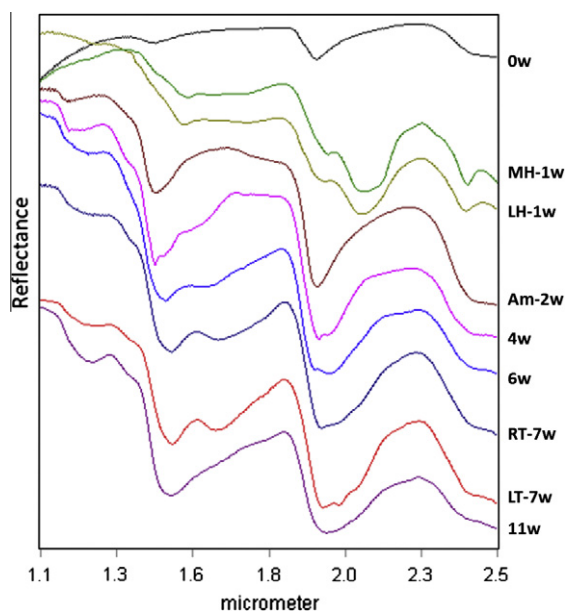


Fig. 17. NIR reflectance spectra (1.1–2.5 μm) of Mg-sulfates with different degrees of hydration, to be compared with the spectra obtained from Mars orbital remote sensing spectrometers (OMEGA & CRISM). Spectra were shifted vertically to show the detailed spectral features. NIR spectrum of LT-7w (red color) shows better resolved peaks in 1.4–1.7 μm range with stronger 1.6 μm peak, and three fine spectral features in 1.9–2.2 μm range when compared with that of RT-7w. NIR spectrum of LH-1w (green color) shows a shifted 2.4 μm band and flat-top 2.1 μm band when compared with that of MH-1w. The bands in the spectrum of 0w are from adsorbed water. Modified from Fig. 4 of Wang et al. (2011).

The data from the Spirit and Opportunity rovers (in equatorial regions) and the Phoenix Lander (in the polar region) did suggest the existence of Mg sulfates with undetermined hydration states in subsurface regolith. Based on the subsurface temperature profile from thermal modeling (Mellon et al., 2004), and the high values of WEH (Water Equivalent Hydrogen) identified by Neutron Spectrometry (Feldman et al., 2004) on the Mars Odyssey within the two equatorial regions where Spirit and Opportunity explored, we cannot exclude the existence of Mg sulfates with the highest hydration states, i.e., meridianiite (11w) and LT-7w, in subsurface (Wang, 2012; Wang et al., 2012b).

The formation of amorphous Mg sulfates was observed during the dehydration experiments on epsomite (7w) and hexahydrate (6w), but not on starkeyite (4w) (Vaniman et al., 2004; Wang et al., 2006). Amorphous Mg sulfates can remain unchanged for a long period of time in a low RH (5–11%) environment at $T > 5$ °C (Wang et al., 2009), but will rehydrate to LT-7w under the similar RH at $T < -10$ °C (Wang et al., 2011). The highest water content of an amorphous Mg-sulfate structure is three water molecules per MgSO₄ unit (Wang et al., 2009).

However, the likelihood of forming amorphous Mg sulfates during a diurnal cycle at moderate obliquity period on Mars is very low based on the rate ratios (to be discussed in Section 6.2.2.3.). The critical condition to form amorphous Mg sulfates is to rapidly extract H₂O from Mg sulfates with high degrees of hydration in high to median temperature range (50 °C to 0 °C in Wang et al., 2006, 2009), thus causing collapse of their crystalline structures. At a much lower temperature, the amorphization would need to compete with the 7w → 4w dehydration process (as observed in a vacuum desiccation experiment at -8 °C, Wang et al., 2009). More importantly, the rates of formation of epsomite, the starting phase for amorphization, from the rehydration of LH-1w and 4w at low temperature (~ 180 K at the early morning at the surface of Mars) during the current moderate obliquity period on Mars are extremely slow. We therefore concluded that the amorphous Mg sulfates should not be considered a common Mg-sulfate phase to be found at the Martian surface (Wang et al., 2011). Our conclusion contradicts that of Vaniman et al. (2004), who suggested amorphous Mg sulfates can be a common phase due to the rapid dehydration in the diurnal cycle (i.e., RH change) in moderate obliquity periods; the reaction rate was not considered in their discussion.

6.2.2.3. The extraction of reaction rate information. In principle, information on the reaction rates of dehydration/rehydration processes associated with Mg sulfate hydrates can be derived from the results of our experiments on stability field and phase-transition pathways, including the 120 experiments published in Wang et al. (2009) at 5 °C, 21 °C, and 50 °C, and the 30 experiments at -10 °C published in Wang et al. (2011). Specifically, the data on the phases identified (by Raman spectroscopy) in the reaction products at intermediate stages and the hours (since placement of starting hydrates into RH buffers) needed for the appearance of new phases of dehydration or rehydration are critical for the rate calculation. However, our experiments were originally designed to investigate stability fields; the parameters used and the frequency of phase identification at intermediate stages of experiments were fixed. Also, because of their long duration, repeating these experiments is not an option. Accordingly, there are uncertainties in the rate calculations (discussed in Wang et al., 2011), thus only rough estimates of the reaction rates can be made from these data. In fact, we consider only the order of magnitude of reaction rate ratios.

The data points marked by solid triangles in $\ln(1/t)$ (s) versus $1/T$ (K) in Fig. 18 are from our experiments, those in open triangles are extrapolations to lower temperatures relevant to Mars surface and subsurface conditions. Fig. 18 demonstrates that our experimental results match very well with the Arrhenius equation:

$$\ln(k) = \ln(A) - \frac{E_a}{R} \left(\frac{1}{T} \right), \quad (16)$$

where k is the rate constant, A is a pre-exponential factor, E_a is activation energy, R is the gas constant, and T is absolute temperature (K). In these plots, the rate constant $k = 1/t$, where t is the time (in s) needed for a total phase conversion (e.g., $7w \rightarrow 4w$). A linear regression line was derived from the three experimental data sets (50 °C, 21 °C, 5 °C) of each five dehydration and rehydration processes. The slope and intersection from each regressed line were then used in extrapolation of the rates for that process.

Because all samples (except meridianiite) were prepared in the same way, the effects of grain size and sample porosity on reaction rates can be excluded. Fig. 18 shows that the reaction rates of all five processes are all strongly affected by temperature, i.e., they decrease as temperature decreases. Fig. 18 also shows that among the trends of rate-constant change as a function of temperature for all five processes, the rates of two dehydration reactions ($7w \rightarrow 4w$ and $7w \rightarrow Am$) decrease much faster (with temperature decreases)

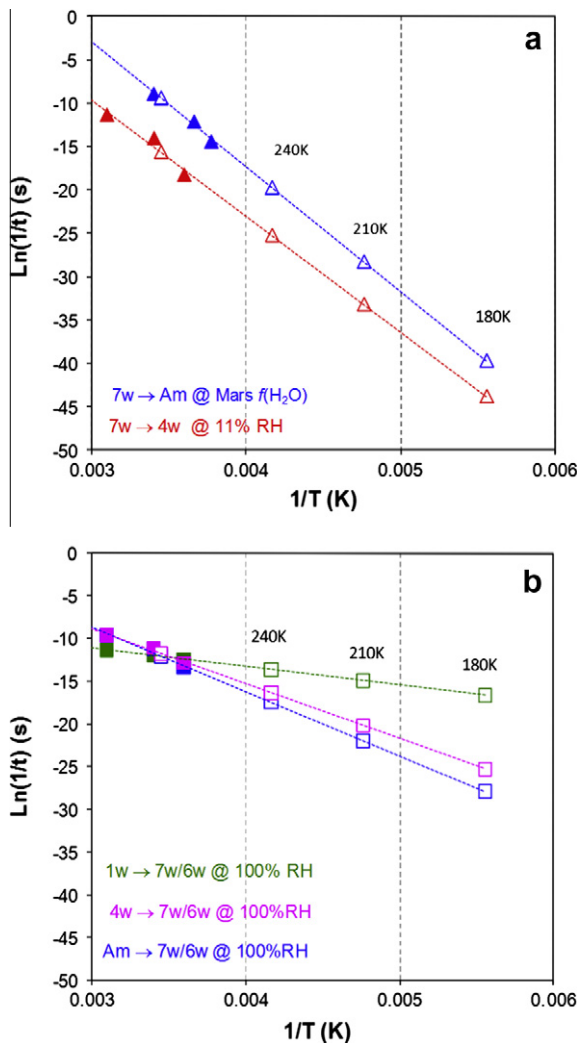


Fig. 18. Correlation between the reaction rate $\ln(1/t)$ and temperature $1/T$ of five dehydration and rehydration processes of Mg-sulfates. The slope and intersections obtained from experimental data (solid triangles) are used to extrapolate the correlations to low temperatures relevant to Mars surface and subsurface. The extrapolated data points are shown as open triangle symbols. Modified from Fig. 10 of Wang et al. (2011).

than those of three rehydration reactions ($4w$, $LH-1w$, and $Am \rightarrow 7w/6w$).

This phenomenon can be explained by considering the two different factors that influence the progress of dehydration and rehydration processes: temperature and $f(H_2O)$. We believe that temperature affects the progress of dehydration more significantly, whereas $f(H_2O)$ affects the progress of rehydration more significantly. The effect of temperature is to change the thermal vibrations of atomic or ionic groups in the crystal structure, whereas the effect of $f(H_2O)$ is to change the availability of H_2O molecules in the environment (detailed evidences and discussions in Wang et al., 2011).

As discussed in Wang et al. (2011), the rate ratios at different temperatures are scientifically meaningful because the uncertainties involved in estimating reaction rates do not affect the general trend (i.e., the slope) of a regression line. Moreover, considering the differences in our experimental setting from the real conditions on Mars (surface and subsurface) and the uncertainties associated with further extrapolation, only the order of magnitude differences in the rate ratios will be considered. Table 6 lists the rate ratios in the form of the order of magnitude, for two important dehydration reactions ($7w \rightarrow 4w$ and $7w \rightarrow Am$, Fig. 18a) and three rehydration reactions ($LH-1w \rightarrow 7w/6w$, $4w \rightarrow 7w/6w$, and $Am \rightarrow$ crystalline $7w/6w$, Fig. 18b), compared to the same type of reactions at 294 K (21 °C).

On the basis of data in Table 6, we can say that when temperature drops to ~ 240 K (-33 °C) as it does during the early evening hours on Mars in equatorial regions, the dehydration of epsomite ($7w$) would slow considerably because the dehydration rate would only be 10^{-5} times (Column 5 in Table 6) the rate at 294 K (21 °C) (Column 3 in Table 6). This rate corresponds to a 2984-yr duration to make the $7w \rightarrow 4w$ transition, which occurs in 351 h at 21 °C and 11% RH in our laboratory setting. Similarly, when temperature drops to ~ 180 K (-93 °C) during the early morning hours on Mars in equatorial regions, the rehydration rates of $LH-1w$, $4w$, and Am (Column 7 in Table 6) would be extremely low, e.g., 10^{-7} – 10^{-8} times the rates at 294 K (21 °C) for the rehydration of Am and $4w$ (Column 3 in Table 6).

6.2.2.4. Understanding Martian Magnesium sulfates. By extrapolating these rate constants into the T range relevant to Mars, we can evaluate the possibility of occurrence of specific processes and the presence of common Mg sulfate species on Mars in different periods and locations. We anticipate in a moderate obliquity period, starkeyite and $LH-MgSO_4 \cdot H_2O$ should be the two most common Mg sulfates at the surface, another polymorph $MH-MgSO_4 \cdot H_2O$ can exist at the locations where hydrothermal or other high temperature processes may have occurred. In polar regions or within the subsurface of low latitude regions, meridianiite (co-existing with water ice, near 100% RH) and $LT-7w$ (over a much wider RH range) are the stable phases. During a high obliquity period, meridianiite and $LT-7w$ should be widespread. The correlations of reaction rates with temperature discussed above imply that dehydration and rehydration of hydrous Mg sulfates would always be slower than the sublimation and crystallization of water ice. We have built a quantitative relationship between Martian obliquity cycle (Laskar et al., 2004) and the retained structural water in Mg-sulfates (based on the dehydration/rehydration rate ratios developed through above experiments (Wang, 2012; Wang et al., 2012b)). It suggests that within the salt-rich subsurface at low environmental T (175–185 K) (Mellon et al., 2004), certain amounts (exact % depends on the actual T) of structural H_2O would remain until today. Therefore, hydrous sulfates can be the major hosts for the high levels of Water-Equivalent-Hydrogen (WEH) found at two large equatorial regions on Mars, by Neutron Spectrometer on Mars Odyssey (Feldman et al., 2004; Maurice et al., 2011).

Table 6

Reaction rate ratios (order of magnitude) of five dehydration and rehydration processes of Mg-sulfates important for Mars sulfate mineralogy. Data in four columns at the right side of this table are rate ratios at four Mars relevant temperatures against the rates at 294 K (21 °C). These ratios were obtained through the extrapolations of rate constant versus *T* correlation shown in Fig. 6.5. Italic font marks the rate ratios during a period when the specific dehydration or rehydration process would be favored at the RH conditions on Mars.

	Duration (h) at 294 K	Rate (1/s) at 294 K	Daytime on Mars		Nighttime on Mars	
			290 K	240 K	210 K	180 K
			Rate ratios against the rates at 294 K			
Temperature			290 K	240 K	210 K	180 K
Duration in hours at Gusev (Smith et al., 2004, 2006)			>10	1–2	1–2	1–2
Estimated RH values based on the work of Smith (2002)			~0%	<1%	1–10%	~100%
Dehydrations						
7w → 4w at 11% RH	351	8E–07	4E–01	1E–05	5E–09	1E–13
7w → Am at <0.1% RH	2	1E–04	6.E–01	3E–05	6E–09	9E–14
Rehydrations						
4w → 6w/7w at 100% RH	19	1E–05	7E–01	5E–03	1E–04	7E–07
1w → 6w/7w at 100% RH	44	6E–06	1E+00	2E–01	5E–02	9E–03
Am → crystalline at 100% RH	21	1E–05	1E+00	2E–03	2E–05	6E–08

6.3. Experiments on the stability field, phase transition pathways, and phase boundaries of Fe³⁺ sulfates

6.3.1. Experiments in three stages

Compared with the study of the stability fields and phase transitions of Mg sulfates (Wang et al., 2009, 2011), a major complication in the study of ferric sulfates is that there are three types of hydrous ferric sulfates (normal, basic, and acidic, such as Fe₂(SO₄)₃·7H₂O, Fe_{4.67}(SO₄)₆(OH)₂·20H₂O, and FeH(SO₄)₂·4H₂O, respectively) and the possible transitions among them (Chipera et al., 2007a, 2007b).

Our study on ferric sulfates has also been conducted in three stages. First (Ling et al., 2008; Ling and Wang, 2010), eight common ferric sulfates were synthesized, with their structures confirmed by X-ray diffraction, and the standard Raman, Vis–NIR (0.4–2.5 μm), and MIR (2.5–25 μm) spectra taken on the same samples. During the second stage (Wang and Ling, 2011; Wang et al., 2012a), five of these synthesized ferric sulfates, including ferricopiapite [Fe_{4.67}(SO₄)₆(OH)₂·20H₂O] (abbreviated as Fe20w in following text and figures), kornelite [Fe₂(SO₄)₃·7H₂O (abbreviated as Fe7w), a crystalline and an amorphous pentahydrated ferric sulfate [Fe₂(SO₄)₃·5H₂O] (abbreviated as Fe5w and FeAm-5w), and rhomboclase [FeH(SO₄)₂·4H₂O] (abbreviated as Fe4w), were used as the starting phases for a set of 150 experiments to study their stability fields and transition pathways at three temperatures (50 °C, 21 °C, and 5 °C) and ten RH levels from 6% to 100%. The preliminary results obtained in second stage provided the constraints on the locations of solid–solid phase boundaries in this *T*–RH space among different hydrous ferric sulfates, which form the basis to design one of the third stage experiments, i.e., to determine the phase boundaries between two ferric sulfates: kornelite [Fe₂(SO₄)₃·7H₂O] and pentahydrate ferric sulfate [Fe₂(SO₄)₃·5H₂O] (Kong et al., 2011a).

6.3.2. Results and discussions

6.3.2.1. Boundaries of deliquescence zones of five ferric sulfates. The approximate positions of boundaries of deliquescence zones (Fig. 19) for the tested five ferric sulfates are determined based on the identification of final phases in 150 dehydration/rehydration experiments (Wang et al., 2012a). Note our experiments were designed to find the approximate locations of the stability fields for the ferric sulfates in which ten discrete RH levels were used at each of the three temperatures, therefore the boundary of deliquescence zones found is expressed in a range of RH values. For example, we observed the deliquescence of ferricopiapite at 76% RH at 5 °C and the unchanged ferricopiapite at 73% RH at 5 °C. Thus the RH range of 73–76% would be the estimated boundary of the

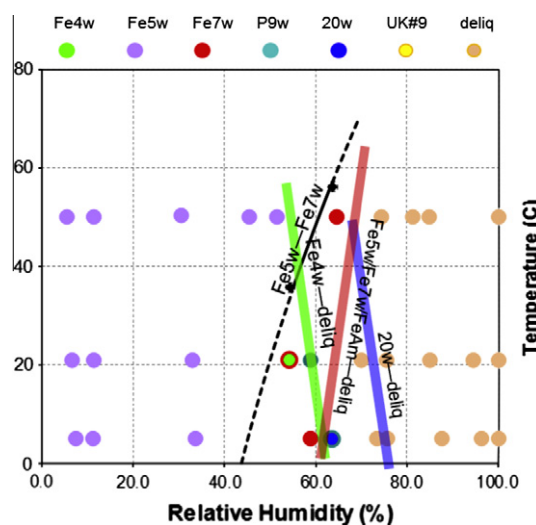


Fig. 19. The estimated boundaries of deliquescence zones of 20w, Fe4w, and Fe5w/Fe7w/FeAm-5w based on the current study, and the Fe5w–Fe7w phase boundary determined by Kong et al. (2011a). 20w = ferricopiapite, Fe4w = rhomboclase, Fe5w = Fe₂(SO₄)₃·5H₂O, Fe7w = kornelite, FeAm-5w = amorphous ferric sulfate with five structural water, P9w = paracoquimbite, UK#9 = a hydrous ferric sulfate with distinct Raman spectrum of unknown structure, deliq = deliquescence.

deliquescence zone at 5 °C for ferricopiapite. Connecting the three RH ranges at three tested temperatures (50 °C, 21 °C, and 5 °C), the estimated boundary of the deliquescence zone for each ferric sulfate species would be a thick line that goes through a space in *T*–RH field (dark blue thick line in Fig. 19).

The estimated boundaries of the deliquescence zones of Fe20w, Fe4w, and Fe7w/Fe5w/FeAm-5w, were drawn in Fig. 19 (as blue colored, green colored and red colored straight thick lines, respectively). Because we have found that ferricopiapite was the necessary pathway in the deliquescence process of both Fe7w and Fe5w, the boundary location of Fe5w/Fe7w – deliquescence (red colored band) should be considered as the location of Fe5w/Fe7w–Fe20w – deliquescence boundary. The fact that this boundary occurs at the lower RH side of the Fe20w – deliquescence boundary at 21 °C to 5 °C, suggests that Fe7w, Fe5w, and FeAm have a narrow RH stability field at mid-low *T*, compared with ferricopiapite (Fe20w).

Similarly, the Fe4w – deliquescence boundary occurs at lower RH side of Fe20w – deliquescence boundary in full tested *T* range (5–50 °C). It suggests a narrower RH stability field of Fe4w than that of Fe20w.

6.3.2.2. Zones of stability fields of five ferric sulfates. On the basis of the phase identification made by Raman spectroscopy at the final and intermediate stages of 150 dehydration/rehydration experiments, we can estimate the general locations and expansions of the stability fields, in $50\text{ }^{\circ}\text{C} \leq T \leq 5\text{ }^{\circ}\text{C}$ range, for the species that were used as starting phases and that appeared frequently (e.g., paracoquimbite, abbreviated as P9w) in these experiments, as shown in Fig. 20a and b.

The variations in reactions rates at different temperatures can bring uncertainty, i.e., the slow rates of certain reactions can cause the lack of equilibrium, even after a reasonably long laboratory experiments (>4 years), thus the phase remains metastable for long time. For this reason, we used the shades of color in Fig. 20a and b to present the confidence levels of our study on the different parts of stability field. For example, a dark purple shade (high confidence) was used in the zone of 6–65% RH and $50\text{ }^{\circ}\text{C}$ for the stability field of Fe5w, a light purple shade (less confidence) was used for 7–33% RH and $5\text{--}21\text{ }^{\circ}\text{C}$. Defining the exact locations of stability fields of a ferric sulfate is dependent on defining all surrounding phase boundaries, such as the study for hexahydrated Mg sulfate by Chou and Seal (2003a).

6.3.2.3. Two new phases in the series of $\text{Fe}_2(\text{SO}_4)_3 \cdot x\text{H}_2\text{O}$. Kornelite (Fe7w) (Robinson and Fang, 1973) contains layers consisting of a

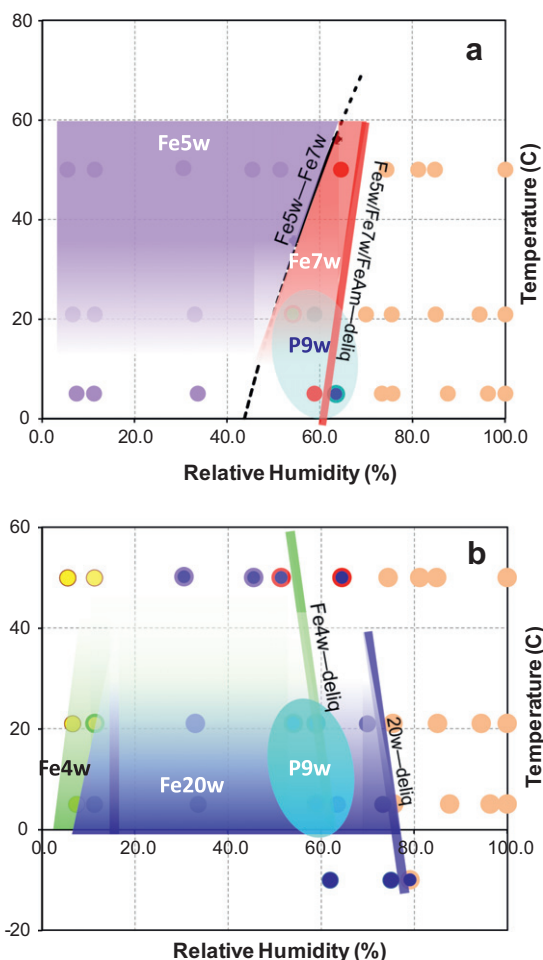


Fig. 20. (a) Stability and metastability fields of Fe5w, Fe7w, and P9w, with the shades of color representing the confidence levels. The estimated boundaries for the deliquescence zones of Fe5w and Fe7w (through 20w) are also shown. (b) Estimated stability fields of ferricopiapite (20w), rhomboclase (Fe4w) and paracoquimbite (P9w), with the shades of color to representing the confidence levels. The estimated boundaries for the deliquescence zones of 20w and Fe4w are also shown. Modified from Fig. 15 of Wang et al. (2012).

network of $[\text{SO}_4]$ tetrahedra and $[\text{Fe}(\text{OH}_2)_3\text{O}_3]$ octahedra perpendicular to c axis. With the six structural waters per molecule directly coordinated with Fe^{3+} , the remaining structural water molecules occur among the layers, and they are bonded by much weaker hydrogen bonding into the framework. Different numbers of interlayer structural waters were reported for kornelite: 1.25w by Robinson and Fang (1973), 1.0w by Posnjak and Merwin (1922), and 1.75w by Ackermann et al. (2009). Furthermore, we have found (Ling and Wang, 2010) that this number can be 2.0, i.e., a hydrous ferric sulfate with eight structural waters $[\text{Fe}_2^{3+}(\text{SO}_4)_3 \cdot 8\text{H}_2\text{O}]$. It was synthesized from an amorphous pentahydrated ferric sulfate at $95\text{ }^{\circ}\text{C}$ and 30.5% RH (controlled by MgCl_2 RH buffer). The product has a XRD pattern quite similar to kornelite, but a very distinct Raman spectral pattern (Fig. 21a).

When the number of interlayer structural water goes to zero $[\text{Fe}_2^{3+}(\text{SO}_4)_3 \cdot 6\text{H}_2\text{O}]$, the structure is called lausénite (Robinson and Fang, 1973). Majzlan et al. (2005) reported a crystal structure of pentahydrated ferric sulfate $[\text{Fe}_2^{3+}(\text{SO}_4)_3 \cdot 5\text{H}_2\text{O}]$, in which Fe has two octahedral sites with different types of coordinates: $[\text{Fe}(\text{OH}_2)_3\text{O}_3]$, and $[\text{Fe}(\text{OH}_2)_2\text{O}_4]$. We were able to synthesize both lausénite and a pentahydrated ferric sulfate (Ling and Wang, 2010). We confirmed that our synthesized pentahydrated ferric sulfate has the same XRD pattern as that of Majzlan et al. (2005) and a characteristic Raman spectrum shown in Fig. 21d. In addition, we synthesized a hexahydrated ferric sulfate (Ling and Wang, 2010). This hexahydrated ferric sulfate has a pale yellowish color, a distinct XRD pattern with no match in the PDF2006 database, and a distinct Raman spectrum (Fig. 21c) that is different from those of heptahydrated $[\text{Fe}_2^{3+}(\text{SO}_4)_3 \cdot 7\text{H}_2\text{O}]$ (Fig. 21b), octahydrated $[\text{Fe}_2^{3+}(\text{SO}_4)_3 \cdot 8\text{H}_2\text{O}]$, and pentahydrated $[\text{Fe}_2^{3+}(\text{SO}_4)_3 \cdot 5\text{H}_2\text{O}]$ ferric sulfates.

More importantly, these two ferric sulfates appeared in the products of intermediate stages during the dehydration/rehydration reactions started from kornelite (Fe7w) and amorphous pentahydrated ferric sulfate (FeAm-5w), which imply that these phases are independent hydrous ferric sulfates with their own role in the pathways of the phase transitions among other hydrous ferric sulfates.

6.3.2.4. Structural water maintained by amorphous ferric sulfates and the thin film of water attached on ferricopiapite grains. Amorphization was observed during the dehydration of ferricopiapite and in the precipitation from $\text{Fe}^{3+}\text{--}\text{SO}_4\text{--}\text{H}_2\text{O}$ brine at specific T and RH conditions. The range of structural waters that can be held by

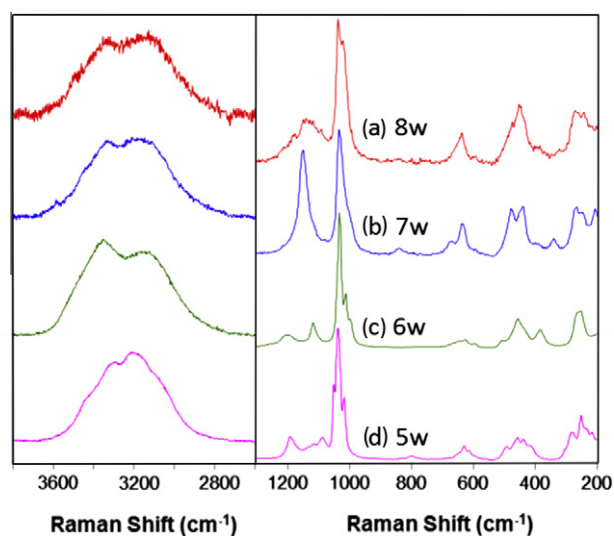


Fig. 21. Characteristic Raman spectra obtained from (a) octahydrated (8w) and (d) pentahydrated ferric sulfates (5w) compared to Raman spectra of (b) kornelite (7w) and (c) lausénite (6w). Modified from Fig. 9 of Wang et al. (2012).

FeAm structure was evaluated through a set of experiments run under a set of T and RH conditions. It was determined the maximum amount of structural water that can be held by Am structure at 33.6% RH and 5 °C is eleven H_2O molecules per $Fe_2(SO_4)_3$, i.e., a H_2O to SO_4 ratio of 3.7 comparable with that (~ 3.5) in crystalline ferricopiapite. The variations in water content of a FeAm structure are directly expressed in the central position of its ν_1 Raman peak, from 1035.1 cm^{-1} to 1020.2 cm^{-1} . The tight correlation between Raman ν_1 peak position and the number of structural water per amorphous $Fe_2(SO_4)_3$ unit was found with a $R > 0.99$ (Fig. 22, a $R > 0.76$ represents a confident level of 99.9% for 15 data points).

During our investigation, gravimetric measurements were made on the products of final and intermediate stages of dehydration/rehydration reactions, where the number of H_2O per molecule of specific ferric sulfate was calculated and compared with the phase identification made by Raman spectroscopy. The gravimetric measurements of the intermediate products at mid RH levels (65–75%) at 21–5 °C which started with ferricopiapite indicate that the H_2O per ferricopiapite molecule increased from 20 to 26.8 and 32.5 (5 °C, Fig. 23a), or from 20 to 28.4 and 30.9 (21 °C). The Raman spectra (vibrational modes for SO_4 and H_2O/OH) obtained from these samples indicate the materials kept a typical ferricopiapite structure as reflected by a distinctly different spectrum compared to that of a Fe^{3+} - SO_4 aqueous solution.

These observations suggest that the extra H_2O (max $\sim 12.5w$ /molecule at 5 °C, max $\sim 10.9w$ /molecule at 21 °C) must occur at the surface of ferricopiapite grains as adsorbed water. This extra water at the surface of ferricopiapite grain would form a liquid-water film with considerable thickness. Assuming a closest packing of ferricopiapite molecules in a spherical grain of 10 μm diameter, an extra 12.5w per ferricopiapite molecule at 5 °C would correspond 2090 layers of H_2O molecules at its surface.

A film of liquid water with this thickness should be macroscopically observable. Fig. 23b–d show the photos of a set of samples from the experiments at 5 °C: ferricopiapite equilibrated at 7% RH with no obvious “extra” H_2O shown as fine powder (Fig. 23b); when equilibrated at 64% RH (Fig. 23c), it showed as clustered grains (extra 6.8 H_2O per molecule, Fig. 23a); and when equilibrated at 73% RH (Fig. 23d), it showed as paste with shiny surface (extra 12.5 H_2O per molecule, Fig. 23a). Note all these

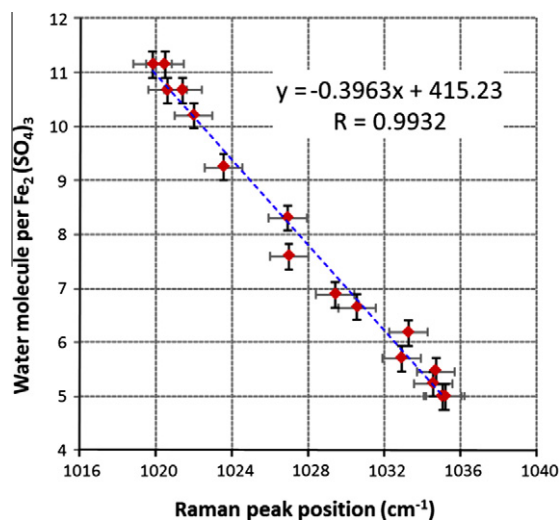


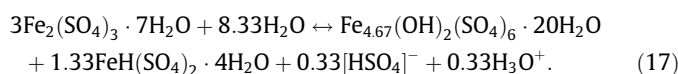
Fig. 22. Raman peak position shifts during a rehydration process of FeAm-5w at 34% RH and 5 °C. The regression line shows a tight correlation ($R > 0.99$) between the central position of Raman peak (cm^{-1}) and the number of structural water per $Fe_2(SO_4)_3$ molecule, determined by gravimetric measurements. Notice a $R > 0.76$ would represent a confident level of 99.9% for 15 data points. Modified from Fig. 14 of Wang et al. (2012).

samples maintained the characteristic Raman spectrum of ferricopiapite.

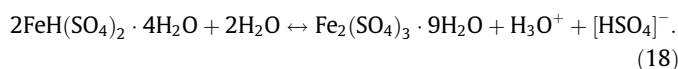
6.3.2.5. *Phase transition among normal, basic, and acidic ferric sulfates.* Our experiments placed the starting ferric sulfates in an environment where only T and RH change (i.e., no pH change). A strictly hydration or rehydration reaction should cause changes among phases with different hydration degrees, but not affect their acidities, e.g., the hydration/dehydration among normal ferric sulfates with Fe5w, Fe7w, and Fe9w are possible, but the phase transition across different types of ferric sulfates (normal, basic, and acidic,) should not easily happen. Nevertheless, we have observed these types of phase transitions in our experiments: such as the transfer from ferricopiapite to rhomboclase (basic to acidic, and vice versa).

The equations of these phase transitions can be:

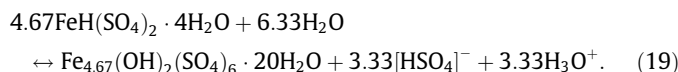
Normal to/from basic sulfates (e.g., Fe7w \leftrightarrow Fe20w)



Acidic to/from normal sulfates (e.g., Fe4w \leftrightarrow Fe9w)



Acidic to/from basic sulfates (e.g., Fe4w \leftrightarrow Fe20w)



These solid–solid phase transitions involve the change of $Fe^{3+}:[SO_4]^{2-}$ ratio in a solid phase. We believe that can only happen if certain amount of Fe^{3+} or $[SO_4]^{2-}$ was removed from solid phases. On the basis of observations described in 6.3.2.4, i.e., at mid-high RH levels, thin film of H_2O can form at the surface of a ferricopiapite grain. This thin film of H_2O can host the ions like Fe^{3+} , $[H_3O]^+$, $[SO_4]^{2-}$, $[HSO_4]^-$, thus changing the $Fe^{3+}:[SO_4]^{2-}$ ratios in solid phases and making the phase transitions (1, 2, 3) possible at those RH levels. Fe4w, Fe7w, and Fe5w are less capable than ferricopiapite in holding adsorbed H_2O . In our experiments, they were found to be able to hold ~ 1 extra H_2O /molecule under the same conditions when ferricopiapite can hold 6.8–12.5 extra H_2O /molecule. This water layer can facilitate the movement of Fe^{3+} , $[H_3O]^+$, $[SO_4]^{2-}$, and $[HSO_4]^-$ ions.

6.3.2.6. *Determination of a phase boundary.* The results of our second stage of the study on hydrous ferric sulfates place an overall view (although incomplete) of the phase relationships among several normal, basic, and acidic hydrous ferric sulfates, in a wide T - RH space relevant to Mars surface and subsurface conditions (Figs. 19 and 20). In order to refine the phase boundaries among them, and especially to build a more detailed understanding of their behavior on Mars, many follow-up experiments have to be designed and conducted. We have accomplished the determination of a phase boundary between kornelite (Fe7w) and pentahydrated (Fe5w) ferric sulfate (Fig. 20a, first published by Kong et al., 2011a) using the experimental parameters selected based on the second stage experiments. The experiments to determine the phase boundary between kornelite (7w), paracoquimbite (9w), and ferricopiapite (Fe20w) at lower temperatures are planned for future investigations.

6.3.2.7. *Understanding Martian iron sulfates.* Ferric sulfates were observed on Mars, especially at the Gusev and Meridiani sites explored by the Spirit and Opportunity Rovers. With exception of

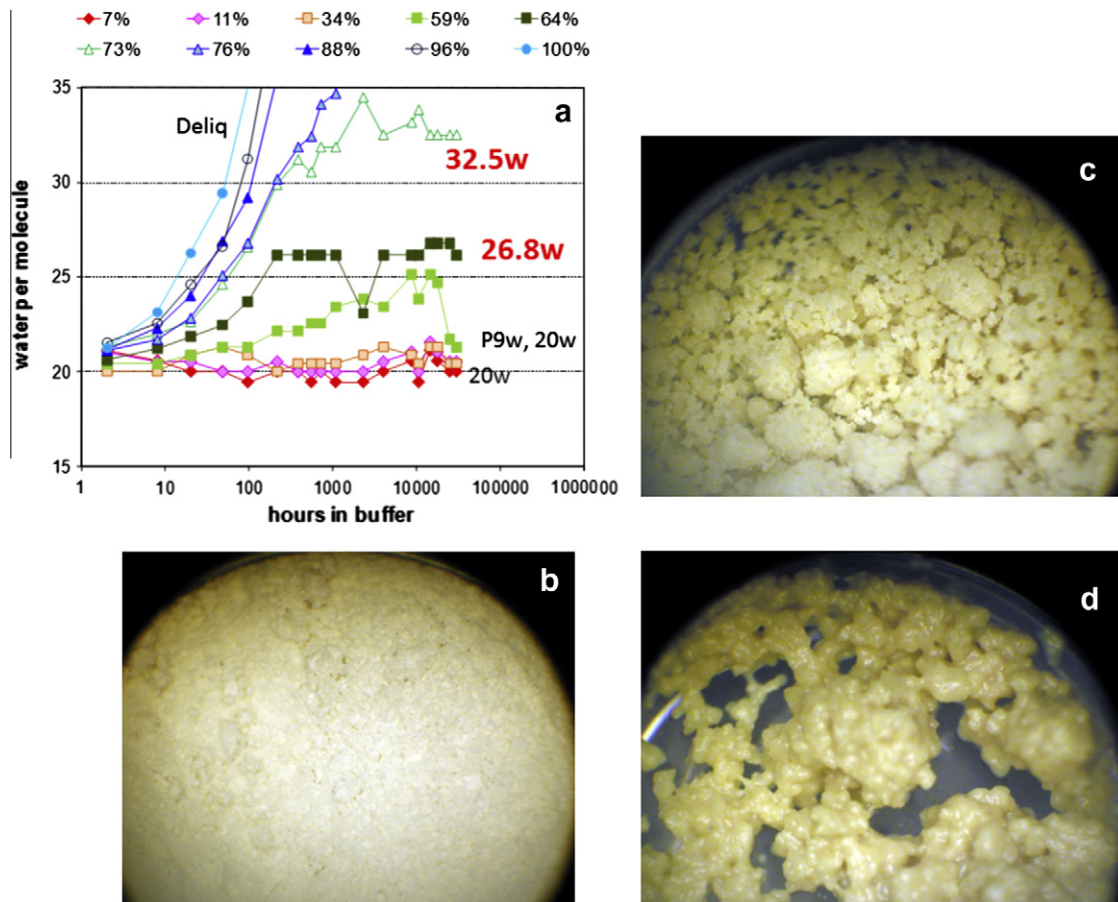


Fig. 23. (a) Changes in the number of structural waters per ferricopiapite formula unit calculated from gravimetric measurements of final and intermediate reaction products of 30 experiments started from ferricopiapite at 5 °C; (b) Ferricopiapite equilibrated at 5 °C in 7% RH (LiBr–H₂O buffer) – fine powder; (c) Ferricopiapite equilibrated at 5 °C in 64% RH (NaBr–H₂O buffer) – clusters; (d) Ferricopiapite equilibrated at 5 °C in 73% RH (KI–H₂O buffer) – shiny paste. Modified from Figs. 4a and 6a–c of Wang et al. (2012).

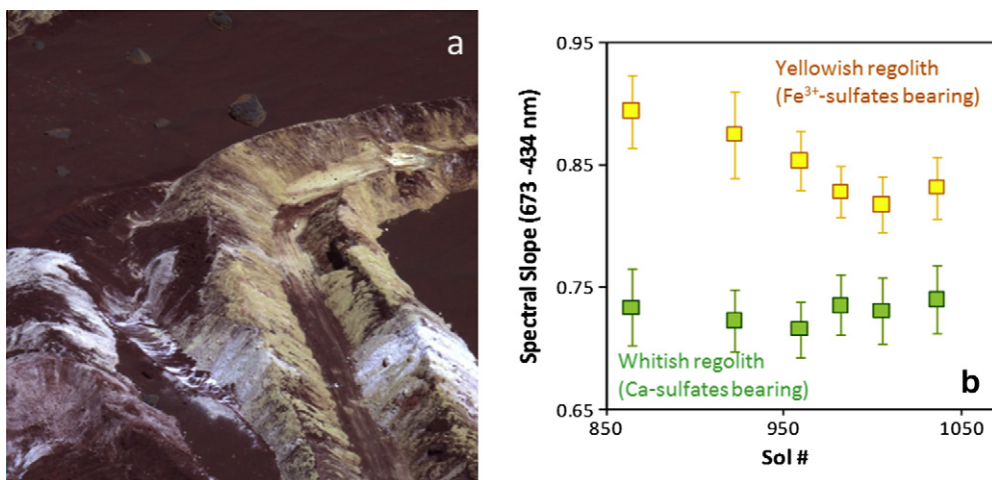


Fig. 24. Subsurface regolith enriched Ca-sulfates and Fe³⁺-sulfates were excavated by the Spirit rover at Tyrone site in Gusev Crater on Mars. (a) Multicolor Pancam image of Tyrone excavated subsurface regolith; (b) Quantification of the spectral variations among the six Pancam Tyrone monitoring observations, showing the change of spectral slopes (434 nm to 673 nm) of Fe³⁺-sulfate-rich regolith from tens' cm depth after its exposure to Mars current atmospheric conditions at surface. Modified from Figs. 2a and 10d of Wang and Ling (2011).

the definitive mineral identification of jarosite (Klingelhofer et al., 2004), most occurrences of iron sulfates in those two sites were determined by Mössbauer spectral analyses to be unspecified ferric sulfates (Morris et al., 2006, 2008), with a few suggested ferric sulfate species based on Vis–NIR spectral deconvolution (Johnson et al., 2007). In addition, a two-layer salty soil was excavated by

the Spirit rover at the Tyrone site in Gusev crater (Fig. 24a). The lower layer of yellowish-colored salty soil (that was originally buried beneath the surface basic soil and a Ca-sulfate-rich whitish-colored salty soil layer) contains 37% of ferric sulfates, with ferricopiapite as the major component (suggested by Johnson et al., 2007).

After being exposed to current Martian atmospheric conditions for 198 sols, a color change of yellowish salty soil was observed. In the Vis–NIR spectra extracted from seven systematic multi-color Pancam observations, a reduction of spectral slope from 434 to 753 nm was observed from the yellowish Fe–sulfate–rich soil (Fig. 24b, details in Wang and Ling, 2011). On the basis of the results presented in this manuscript, especially the occurrence of the dehydration processes from ferricopiapite, we conclude that the phase transitions from ferricopiapite to rhomboclase, and to amorphous and quasi-amorphous ferric sulfates are the most likely cause for spectral change in VIS–NIR spectra of Tyrone ferric sulfates.

As revealed in Fig. 20, ferricopiapite is stable in a wide *RH* range at mid-low temperature (5 °C to 21 °C), and also in the to-be-determined stability field at even lower *T* (systematic experiments at –10 °C are ongoing). The observations of ferricopiapite in subsurface regolith and its dehydration after exposure to surface atmospheric condition indicate that its original environment must have the suitable *T* and *RH* conditions that have prevented (or at least slowed down) the dehydration of a highly hydrated ferric sulfate (ferricopiapite).

7. Future research

Significant advance has been made in the last decade on stability and occurrence of sulfate and hydrated sulfate minerals in terrestrial environments and also on Mars (Bish et al., 2003; Chou et al., 2002; Chou and Seal, 2003a,b, 2007; Chipera and Vaniman, 2007a; Chipera et al., 2007b; Cloutis et al., 2006; Grevel and Majzlan, 2009; Kong et al., 2011a,b; Ling and Wang, 2010; Peterson and Wang, 2006; Majzlan et al., 2004, 2005, 2006; Majzlan and Michalik, 2007; Tosca et al., 2007; Vaniman et al., 2004, 2009; Vaniman and Chipera, 2006; Wang, 2012; Wang et al., 2006, 2009, 2011, 2012; Xu et al., 2009), especially on the derivation of an internally consistent set of thermodynamic data for these minerals, the recognition of their presence on Mars, and also their effects on environments. However, all of recent experimental studies were limited to pure end-member minerals containing only one kind of metal in a single valence state, whereas some of natural minerals are in more complicated solid solution states. Future research will need to address solid solution effects in these phases, and investigate mixed valence phase commonly found in natural systems. It remains a challenge to design new experimental methods or theoretical approaches to study these important topics. The catalytic effect of the co-existing Ca sulfates, ferric sulfates, Fe oxides, and Fe hydroxides on the dehydration of Mg sulfates, especially from epsomite to LH-1w was reported by Wang et al. (2009), and we need to consider this effect on the occurrence of other sulfate minerals in nature. Furthermore, our experience on reaction kinetics and reaction rates for hydration or dehydration of these minerals is still quite limited, especially in a much wider temperature and pressure ranges relevant to many planetary bodies. For example, more experimental studies are needed on the stability as well as hydration–dehydration reaction kinetics of sulfate and hydrated sulfate minerals at temperatures below 0 °C. Another example is the pressure effect on the reaction rates of dehydration/rehydration processes of sulfate and hydrated sulfate minerals, as demonstrated by Wang et al. (2011) and McCord et al. (2001) at 1 atm, at *P* < 1 mb, and at ultra-high vacuum for Mg-sulfates, that needs to be further studied for planetary applications.

Acknowledgments

The research of Chou and Seal was funded by the Mineral Resources Program of the U.S. Geological Survey. The studies on the

fundamental properties of hydrous Mg- and Fe³⁺-sulfates under Mars relevant conditions were supported by NASA Mars Fundamental Research Program NNX07AQ34G, NNX10AM89G; NASA Mission of Opportunity Program 1295053; and a special fund by McDonnell Center for Space Sciences at Washington University in St. Louis. The studies of two graduate students during this work were supported by China Scholarship Council and from Shandong University. John Freeman, Zongcheng Ling, Weigang Kong, Pablo Sobron, Michael Jin, and Yanli Lu made contributions in various parts of these studies. We thank Jane Hammarstrom (U.S. Geological Survey), Brendt C. Hyde (Royal Ontario Museum, Canada), and Ronald C. Peterson (Queen's University, Canada) for constructive reviews. The assistance of Natalia Ainsfield with the reference list is greatly appreciated. The use of trade, product, industry, or firm names in this report is for descriptive purposes only and does not constitute endorsement by the U.S. Government.

References

- Ackermann, S., Lazic, B., Armbruster, T., Doyle, S., Grevel, K.D., Majzlan, J., 2009. Thermodynamic and crystallographic properties of kornelite [Fe₂(SO₄)₃·7.75H₂O] and paracoquimbite [Fe₂(SO₄)₃·9H₂O]. *American Mineralogist* 94, 1620–1628.
- Alpers, C.N., Nordstrom, D.K., Thompson, J.M., 1994. Seasonal variations of Zn/Cu ratios in acid mine water from Iron Mountain, California. In: Alpers, C.N., Blowes, D.W. (Eds.), *Environmental Geochemistry of Sulfide Oxidation*. American Chemical Society Symposium Series 550, pp. 324–344.
- Alpers, C.N., Jambor, J.L., Nordstrom, D.K. (Eds.), 2000. *Sulfate Minerals: Crystallography, Geochemistry and Environmental Significance*. Washington, D.C. Mineralogical Society of America, *Reviews in Mineralogy and Geochemistry* 40, pp. 608.
- Alpers, C.N., Nordstrom, D.K., Spitzley, J., 2003. Extreme acid mine drainage from a pyritic massive sulfide deposit: the Iron Mountain end-member. In: Jambor, J.L., Blowes, D.W., Ritchie, A.I.M., (Eds.), *Environmental Aspects of Mine Wastes*, Mineralogical Association of Canada Short Course Series 31, pp. 407–430.
- Anderson, J.L., Peterson, R.C., Swainson, I.P., 2007. The atomic structure and hydrogen bonding of deuterated melanterite, FeSO₄·7D₂O. *Canadian Mineralogist* 45, 457–469.
- Archer, D.G., Rard, J.A., 1998. Isopiestic investigation of the osmotic and activity coefficients of aqueous MgSO₄ and the solubility of MgSO₄·7H₂O(cr) at 298.15 K: thermodynamic properties of the MgSO₄ + H₂O system to 440 K. *Journal of Chemical Engineering Data* 43, 791–806.
- Ávila, P.F., Ferriera da Silva, E., Salgueiro, A.R., Farinha, J.A., 2008. Geochemistry and mineralogy of mill tailings impoundments from the Panasqueira mine (Portugal): implications for the surrounding environment. *Mine Water and the Environment* 27, 210–224.
- Bandy, M.C., 1938. Mineralogy of three sulphate deposits of northern Chile. *American Mineralogist* 23, 669–760.
- Barthel, J., Neueder, R., Poepke, H., Wittmann, H., 1998. Osmotic activity coefficients of nonaqueous electrolyte solutions. 1. Lithium perchlorate in the protic solvents methanol, ethanol, and 2-propanol. *Journal of Solution Chemistry* 27, 1055–1066.
- Bauerek, A., Cabala, J., Smieja-Król, B., 2009. Mineralogical alterations of Zn-Pb flotation wastes of Mississippi Valley-type ores (southern Poland) and their impact on contamination of rainwater runoff. *Polish Journal of Environmental Studies* 18, 781–788.
- Bigham, J.M., Nordstrom, D.K., 2000. Iron and aluminum hydroxysulfates from acid sulfate waters. In: Alpers, C.N., Jambor, J.L., Nordstrom, D.K., (Eds.), *Sulfate Minerals – Crystallography, Geochemistry, and Environmental Significance*. *Reviews in Mineralogy and Geochemistry* 40, pp. 351–403.
- Bigham, J.M., Schwertmann, U., Traina, S.J., Winland, R.L., Wolf, M., 1996. Schwertmannite and the chemical modeling of iron in acid sulfate waters. *Geochimica et Cosmochimica Acta* 60, 2111–2121.
- Bish, D.L., Carey, J.W., Vaniman, D.T., Chipera, S.J., 2003. Stability of hydrous minerals on the martian surface. *Icarus* 164, 96–103.
- Blowes, D.W., Reardon, E.J., Jambor, J.L., Cherry, J.A., 1991. The formation and potential importance of cemented layers in inactive sulfide mine tailings. *Geochimica et Cosmochimica Acta* 55, 965–978.
- Bolte, H., 1912. Untersuchungen über die Dissociation einiger kristallwasserhaltigen Salze. *Zeitschrift für Physikalische Chemie* 80, 338–360.
- Bonnell, D.G.R., Burrig, L.W., 1935. The dissociation pressures of some salt hydrates. *Transactions of the Faraday Society* 31, 473–478.
- Bril, H., Zainoun, K., Puziewicz, J., Courtin-Nomde, A., Vanaecker, M., Bollinger, J.-C., 2008. Secondary phases from the alteration of a pile of zinc-smelting slag as indicators of environmental conditions: an example from Świętochłowice, Upper Silesia, Poland. *Canadian Mineralogist* 46, 1235–1248.
- Buckby, T., Black, S., Coleman, M.L., Hodson, M.E., 2003. Fe-sulphate-rich evaporative mineral precipitates from the Río Tinto, southwest Spain. *Mineralogical Magazine* 67, 263–278.

- Buurman, P., 1975. In vitro weathering products of pyrite. *Geologie en Mijnbouw* 54, 101–105.
- Carmona, D.M., Faz Cano, Á., Arocena, J.M., 2009. Cadmium, copper, lead, and zinc in secondary sulfate minerals in soils of mined areas in southeast Spain. *Geoderma* 150, 150–157.
- Carpenter, C.D., Jette, E.R., 1923. The vapor pressures of certain hydrated metal sulfates. *Journal of the American Chemical Society* 45, 578–590.
- Charles, R.W., Vidale Buden, R.J., Goff, F., 1986. An interpretation of the alteration assemblages at Sulphur Spring, Valles Caldera, New Mexico. *Journal of Geophysical Research* 91, 1887–1898.
- Chipera, S.J., Vaniman, D.T., 2007. Experimental stability of magnesium sulfate hydrates that may be present on Mars. *Geochimica et Cosmochimica Acta* 71, 241–250.
- Chipera, S.J., Vaniman, D.T., Bish, D.L., 2007b. The effect of temperature and water on ferric-sulfates. In: 38th Lunar and Planetary Science Conference, LPI Contribution No. 1338, p. 1409.
- Chou, I.-M., Seal II, R.R., Hemingway, B.S., 2002. Determination of melanterite-rozenite and chalcantite-bonattite equilibria by humidity measurements at 0.1 MPa. *American Mineralogist* 87, 108–114.
- Chou, I.-M., Seal II, R.R., 2003a. Determination of epsomite-hexahydrate equilibria by the humidity-buffer technique at 0.1 MPa with implications for phase equilibria in the system $MgSO_4-H_2O$. *Astrobiology* 3, 619–630.
- Chou, I.-M., Seal II, R.R., 2003b. Acquisition and evaluation of thermodynamic data for morenosite-retgersite equilibria at 0.1 MPa. *American Mineralogist* 88, 1943–1948.
- Chou, I.-M., Seal II, R.R., 2004. Acquisition and evaluation of thermodynamic data for the reaction $CdSO_4 \cdot 8/3H_2O = CdSO_4 \cdot 5/3H_2O$ at 0.1 MPa. *GSA Abstracts with Programs* 36, 337–338.
- Chou, I.-M., Seal II, R.R., 2005a. Acquisition and evaluation of thermodynamic data for Bieberite-moorhouseite equilibria at 0.1 MPa. *American Mineralogist* 90, 912–917.
- Chou, I.-M., Seal II, R.R., 2005b. Determination of goslarite-bianchite equilibria by the humidity-buffer technique at 0.1 MPa. *Chemical Geology* 215, 517–523.
- Chou, I.-M., Seal II, R.R., 2007. Magnesium and calcium sulfate stabilities and the water budget of Mars. *Journal of Geophysical Research* 112, E11004. <http://dx.doi.org/10.1029/2007JE002898>.
- Chouinard, A., Williams-Jones, A.E., Leonardson, R.W., Hodgson, C.J., Silva, P., Téllez, C., Vega, J., Rojas, F., 2005. Geology and genesis of the multistage high-sulfidation epithermal Pascua Au-Ag-Cu deposit, Chile and Argentina. *Economic Geology* 100, 463–490.
- Clegg, S.L., Whitfield, M., 1991. Activity coefficients in natural waters. In: Pitzer, K.S. (Ed.), *Activity Coefficients in Electrolyte Solutions*, second ed. CRC Press, Boca Raton, pp. 279–434.
- Cloutis, E.A., Hawthorne, F.C., Mertzman, S.A., Krenn, K., Craig, M.A., Marcino, D., Methot, M., Strong, J., Mustard, J.F., Blaney, D.L., Bell III, J.F., Vilas, F., 2006. Detection and discrimination of sulfate minerals using reflectance spectroscopy. *Icarus* 184, 121–157.
- Cravotta, C.A., III, 1994. Secondary iron-sulfate minerals as sources of sulfate and acidity. In: Alpers, C.N., Blowes, D.W. (Eds.), *Environmental Geochemistry of Sulfide Oxidation*, American Chemical Society Symposium Series 550, pp. 345–364.
- Dagenhart, T.V., Jr., 1980. The Acid Mine Drainage of Contrary Creek, Louisa County, Virginia: Factors Causing Variations in Stream Water Chemistry. MSc Thesis, University of Virginia, Charlottesville, Virginia.
- Dalton III, J.B., Shirley, J.H., Kamp, L.W., 2012. Europa's icy bright plains and dark lines: Exogenic and endogenic contributions to composition and surface properties. *Journal of Geophysical Research* E03003. <http://dx.doi.org/10.1029/2011JE003909>.
- DeKock, C.W., 1986. Thermodynamic Properties of Selected Transition Metal Sulfates and Their Hydrates. U.S. Bureau of Mines Information Circular 9081.
- Delines, M., 1975. Volcanic sublimates of Rugarama, Kiva region, Republic of Zaire. *Bulletin du Service Géologique de la République du Rwanda* 8, 1–11.
- Diesnis, M., 1935. Sur la détermination des états hygrométriques critiques. *Bulletin de la Société Chimique de France* 5 (2), 1901–1907.
- Dokoupilová, P., Sracek, O., Losos, Z., 2007. Geochemical behaviour and mineralogical transformations during spontaneous combustion of a coal waste pile in Oslavany, Czech Republic. *Mineralogical Magazine* 71, 443–460.
- Dold, B., Fontboté, L., 2001. Element cycling and secondary mineralogy in porphyry copper tailings as a function of climate, primary mineralogy, and mineral processing. *Journal of Geochemical Exploration* 74, 3–55.
- Farkas, I.M., Weiszburg, T.G., Pekker, P., 2009. A half-century of environmental mineral formation on a pyrite-bearing waste dump in the Mátra Mountains, Hungary. *Canadian Mineralogist* 47, 509–524.
- Feldman, W.C., Prettyman, T.H., Maurice, S., Plaut, J.J., Bish, D.L., Vaniman, D.T., Mellon, M.T., Metzger, A.E., Squyres, S.W., Karunatillake, S., Boynton, W.V., Elphic, R.C., Funsten, H.O., Lawrence, D.J., Tokar, R.L., 2004. The global distribution of near-surface hydrogen on Mars. *Journal of Geophysical Research* 109, E09006. <http://dx.doi.org/10.1029/2003JE002160>.
- Footo, H.W., Scholes, S.R., 1911. The vapor pressure of hydrates, determined from their equilibria with aqueous alcohol. *Journal of the American Chemical Society* 33, 1309–1326.
- Frondel, C., Palache, C., 1949. Retgersite $NiSO_4 \cdot 6H_2O$, a new mineral. *American Mineralogist* 34, 188–194.
- Frost, R.L., Wain, D.L., Reddy, B.J., Martens, W., Martinez-Frias, J., Rull, F., 2006. Sulphate efflorescent minerals from El Jaroso ravine, Sierra Almagrera, Spain – a scanning electron microscopic and infrared spectroscopic study. *Journal of Near Infrared Spectroscopy* 14, 167–178.
- Frowein, P.C.F., 1887. Die Dissociation krystallwasserhaltiger Salze. *Zeitschrift für Physikalische Chemie* 1, 5–14.
- Gellert, R., Rieder, R., Bruckner, J., Clark, B.C., Dreibus, G., Klingelhofer, G., Lugmair, G., Ming, D.W., Wanke, H., Yen, A., Zipfel, J., Squyres, S.W., 2006. Alpha particle X-ray spectrometer (APXS): results from gusev crater and calibration report. *Journal of Geophysical Research* 111, E02505. <http://dx.doi.org/10.1029/2005JE002555>.
- Gomes, M.E.P., Favas, P.J.C., 2006. Mineralogical controls on mine drainage of the abandoned Ervedosa tin mine in north-eastern Portugal. *Applied Geochemistry* 21, 1322–1334.
- Greenspan, L., 1977. Humidity fixed points of binary saturated aqueous solutions. *Journal of Research of the National Bureau of Standards – A Physics and Chemistry* B7A, 89–96.
- Grevel, K.-D., Majzlan, J., 2009. Internally consistent thermodynamic data for magnesium sulfate hydrates. *Geochimica et Cosmochimica Acta* 73, 6805–6815.
- Grevel, K.-D., Majzlan, J., 2011. Thermodynamics of divalent metal sulfates. *Chemical Geology* 286, 301–306.
- Haar, L., Gallagher, J.S., Kelly, G.S., 1984. NBS/NRC Steam Tables: Thermodynamic and Transport Properties and Computer Programs for Vapor and Liquid States of Water in SI Units. Hemisphere, Washington, DC, pp. 320.
- Hammarstrom, J.M., Seal II, R.R., Meier, A.L., Kornfeld, J.M., 2005. Secondary sulfate minerals associated with acid drainage in the eastern US: recycling of metals and acidity in surficial environments. *Chemical Geology* 215, 407–431.
- Hawthorne, F.C., Krivovichev, S.V., Burns, P.C., 2000. The crystal chemistry of sulfate minerals. In: Alpers, C.N., Jambor, J.L., Nordstrom, D.K. (Eds.), *Sulfate Minerals – Crystallography, Geochemistry, and Environmental Significance*, Reviews in Mineralogy and Geochemistry 40, pp. 1–112.
- Herd, C.D.K., 2006. Trace elements in MIL 03346 jarosite: a record of martian surface processes? *Martian Sulfates as Recorders of Atmospheric-Fluid-Rock Interactions* LP I, 7012.
- Hogenboom, D.L., Kargel, J.S., Ganasan, J.P., Lee, L., 1995. Magnesium sulfate-water to 400 MPa using a novel piezometer: densities, phase equilibria, and planetological implications. *Icarus* 115, 258–277.
- Hyde, B.C., King, P.L., Dyar, M.D., Spilde, M.N., Aii, A.-M.S., 2011. Methods to analyze metastable and microparticulate hydrated and hydrous iron sulphate minerals. *American Mineralogist* 96, 1856–1869.
- Innorta, G., Rabbi, E., Tomadin, L., 1980. The gypsum-anhydrite equilibrium by solubility measurements. *Geochimica et Cosmochimica Acta* 44, 1931–1936.
- Jambor, J.L., Traill, R.J., 1963. On rozenite and siderotil. *Canadian Mineralogist* 7, 751–763.
- Jambor, J.L., Nordstrom, D.K., Alpers, C.N., 2000. Metal-sulfate salts from sulfide mineral oxidation. In: Alpers, C.N., Jambor, J.L., Nordstrom, D.K. (Eds.), *Sulfate Minerals – Crystallography, Geochemistry, and Environmental Significance*, Reviews in Mineralogy and Geochemistry 40, pp. 303–350.
- Jamieson, H.E., Robinson, C., Alpers, C.N., McCleskey, R.B., Nordstrom, D.K., Peterson, R.C., 2005. Major and trace element composition of copiapite-group minerals and coexisting water from the Richmond mine, Iron Mountain, California. *Chemical Geology* 215, 387–405.
- Jerz, J.K., Rimstidt, J.D., 2003. Efflorescent iron sulfate minerals: paragenesis, relative stability and environmental impact. *American Mineralogist* 88, 1919–1932.
- Joeckel, R.M., Ang Clement, B.J., Van Fleet Bates, L.R., 2005. Sulfate-mineral crusts from pyrite weathering and acid rock drainage in the Dakota Formation and Graneros Shale, Jefferson County, Nebraska. *Chemical Geology* 216, 433–452.
- Johnson, J.R., Bell, J.F., Cloutis, E., Staid, M., Farrand, W.H., McCoy, T., Rice, M., Wang, A., Yen, A., 2007. Mineralogical constraints on sulfur-rich soils from Pancam spectra at Gusev crater, Mars. *Geophysical Research Letters* 34, L13202. <http://dx.doi.org/10.1029/2007GL029894>.
- Keith, D.C., Runnells, D.D., Esposito, K.J., Chermak, J.A., Hannula, S.R., 1999. Efflorescent sulfate salts: chemistry, mineralogy, and effects on ARD streams. In: Tailings Mine Waste '99, Proceedings of 6th International Conference. Balkema, Rotterdam, The Netherlands, pp. 573–579.
- Keith, T.E.C., Casadevall, T.J., Johnston, D.A., 1981. Fumarole encrustations: occurrence, mineralogy, and chemistry. *U.S. Geological Survey Professional Paper* 1250, 239–250.
- Khorasanipour, M., Tangestani, M.H., Naseh, R., Hajmohammadi, H., 2011. Hydrochemistry, mineralogy and chemical fractionation of mine and processing wastes associated with porphyry copper mines: a case study of the Sarcheshmeh mine. *SE Iran: Applied Geochemistry* 26, 714–730.
- Klingelhofer, G., Morris, R.V., Bernhardt, B., Schroder, C., Rodionov, D.S., de Souza, P.A., Yen, A., Gellert, R., Evlanov, E.N., Zubkov, B., Foh, J., Bonnes, U., Kankeleit, E., Gutlich, P., Ming, D.W., Renz, F., Wdowiak, T., Squyres, S.W., Arvidson, R.E., 2004. Jarosite and hematite at Meridiani Planum from Opportunity's Mossbauer spectrometer. *Science* 306, 1740–1745.
- Kong, W.G., Wang, A., Chou, I.M., 2011. Experimental determination of the phase boundary between koronelite and pentahydrated ferric sulfate at 0.1 MPa. *Chemical Geology* 284, 333–338.
- Kong, W.G., Wang, A., Freeman, J.J., Sobron, P.S., 2011b. A Comprehensive spectroscopic study of synthetic Fe^{2+} , Fe^{3+} , Mg^{2+} , Al^{3+} copiapite. *Journal of Raman Spectroscopy*, 743. <http://dx.doi.org/10.1002/jrs.2790>.
- Lane, M.D., Bishop, J.L., Dyar, M.D., King, P.L., Parente, M., Hyde, B.C., 2008. Mineralogy of the Paso Robles soils on Mars. *American Mineralogist* 93, 728–739.

- Laskar, J., Correia, A.C.M., Gastineau, M., Joutel, F., Levrard, B., Robutel, P., 2004. Long term evolution and chaotic diffusion of isolation quantities of Mars. *Icarus* 170, 343–364.
- Lescœur, M.H., 1889. Recherches sur la dissociation des hydrates salins et des composés analogues. *Annales de Chimie et de Physique* 6, 378–403.
- Lichtenberg, K., Arvidson, R., Morris, R., Murchie, S., Bishop, J., Glotch, T., Noe Dobrea, E., Mustard, J., Andrews-Hanna, J., Roach, L., 2009. Stratigraphy and relationship of hydrated minerals in the layered deposits of Aram Chaos, Mars. Lunar and Planetary Science Conference XXXX, Abstract 2326.
- Lichtenberg, K.A., Arvidson, R.E., Morris, R.V., Murchie, S.L., Bishop, J.L., Remolar, D.F., Glotch, T.D., Dobrea, E.N., Mustard, J.F., Andrews-Hanna, J., Roach, L.H., 2010. Stratigraphy of hydrated sulfates in the sedimentary deposits of Aram Chaos, Mars. *Journal of Geophysical Research* 115, E00D17. <http://dx.doi.org/10.1029/2009JE003353>.
- Ling, Z.C., Wang, A.L., 2010. A systematic spectroscopic study of eight hydrous ferric sulfates relevant to Mars. *Icarus* 209, 422–433.
- Ling, Z., Wang, A., Jollif, B., Arvidson, R., Xia, H., 2008. A systematic Raman, mid-IR, and Vis-NIR spectroscopic study of ferric sulfates and implications for sulfates on Mars. Lunar and Planetary Science Conference XXXX, Abstract 1463.
- Linke, W.F., Seidell, A., 1965. Solubility of Inorganic and Organic Compounds, fourth ed., vol. 2. American Chemical Society, Washington, D.C., pp. 1914.
- Lottermoser, B.G., 2005. Evaporative mineral precipitates from a historical smelting slag dump, Río Tinto, Spain. *Neues Jahrbuch für Mineralogie, Abhandlungen* 181, 183–190.
- Majzlan, J.R. et al., 2004. Thermodynamic properties, low-temperature heat capacity anomalies, and single crystal X-ray refinement of hydronium jarosite, $761(\text{H}_3\text{O})\text{Fe}_3(\text{SO}_4)_2(\text{OH})_6$. *Physics and Chemistry of Minerals* 31, 518–531.
- Majzlan, J., Botez, C., Stephens, P.W., 2005. The crystal structures of synthetic $\text{Fe}_2(\text{SO}_4)_3(\text{H}_2\text{O})_5$ and the type specimen of lausenite. *American Mineralogist* 90, 411–416.
- Majzlan, J., Navrotsky, A., McCleskey, R.B., Alpers, C.N., 2006. Thermodynamic properties and crystal structure refinement of ferricopiapite, coquimbite, rhomboclase, and $\text{Fe}_2(\text{SO}_4)_3 \cdot 5\text{H}_2\text{O}$. *European Journal of Mineralogy* 18, 175–186.
- Majzlan, J., Michalik, R., 2007. The crystal structure, solid solutions and infrared spectra of copiapite-group minerals. *Mineralogical Magazine* 71, 553–569.
- Malinin, A.A., Drakin, S.I., Ankudimov, A.G., 1977. Measurement of equilibrium vapour pressure in stepwise dehydration by using saturated reference solutions. *Russian Journal of Physical Chemistry* 51, 1557–1558, Translated from *Zhurnal Fizicheskoi Khimii*.
- Martin, R., Rodgers, K.A., Browne, P.R.L., 1999. The nature and significance of sulphate-rich aluminous efflorescences from the Te Kopia geothermal field, Taupo Volcanic Zone, New Zealand. *Mineral Magazine* 63, 413–419.
- Maurice, S., Feldman, W., Diez, B., Gasnault, O., Lawrence, D.J., Pathare, A., Prettyman, T., 2011. Mars Odyssey neutron data: 1. Data processing and models of water-equivalent-hydrogen distribution. *Journal of Geophysical Research* 116, E11008. <http://dx.doi.org/10.1029/2011JE003810>.
- McCord, T.B., Orlando, T.M., Teeter, G., Hansen, G.B., Sieger, M.T., Petrik, N.G., Keulen, L.V., 2001. Thermal and radiation stability of the hydrated salt minerals epsomite, mirabilite, and natron under Europa environmental conditions. *Journal of Geophysical Research* 106 (E2), 3311–3319.
- McCubbin, F.M., Tosca, N.J., Smirnov, A., Nekvasil, H., Steele, A., Fries, M., Lindsley, D.H., 2009. Hydrothermal jarosite and hematite in a pyroxene-hosted melt inclusion in martian meteorite Miller Range (MIL) 03346: implications for magmatic-hydrothermal fluids on Mars. *Geochimica et Cosmochimica Acta* 73, 4907–4917.
- Mellon, M.T., Feldman, W.C., Prettyman, T.H., 2004. The presence and stability of ground ice in the southern hemisphere of Mars. *Icarus* 169, 324–340.
- Milliken, R.E., Fischer, W.W., Hurowitz, J.A., 2009. Missing salts on early Mars. *Geophysical Research Letters* 36, L11202. <http://dx.doi.org/10.1029/2009GL038558>.
- Milliken, R.E., Bish, D.L., 2010. Sources and sinks of clay minerals on Mars. *Philosophical Magazine* 90, 2293–2308.
- Minakawa, T., Noto, S., 1994. Botryogen from the Okuki mine, Ehime Prefecture, Japan. *Chigaku Kenkyu* 43, 175–179, *Chem Abstr* 123:61439e.
- Ming, D.W., Gellert, R., Morris, R.V., Arvidson, R.E., Brukner, J., Clark, B.C., Cohen, B.A., d'Uston, C., Economou, T., Fleischer, I., Klingelhofer, G., McCoy, T.J., Mittlefehldt, D.W., Schmidt, M.E., Schroder, C., Squyres, S.W., Treguier, E., Yen, A.S., Zipfel, J., 2008. Geochemical properties of rocks and soils in Gusev Crater, Mars: results of the alpha particle X-ray spectrometer from Cumberland Ridge to Home Plate. *Journal of Geophysical Research* 113, E12S39. <http://dx.doi.org/10.1029/2008JE003195>.
- Morris, R.V., Klingelhofer, G., Schroder, C., Rodionov, D.S., Yen, A., Ming, D.W., de Souza, P.A., Fleischer, I., Wdowiak, T., Gellert, R., Bernhardt, B., Evlanov, E.N., Zubkov, B., Foh, J., Bonnes, U., Kankaleit, E., Gutlich, P., Renz, F., Squyres, S.W., Arvidson, R.E., 2006. Mossbauer mineralogy of rock, soil, and dust at Gusev crater, Mars: spirit's journey through weakly altered olivine basalt on the plains and pervasively altered basalt in the Columbia Hills. *Journal of Geophysical Research* 111, E02S13. <http://dx.doi.org/10.1029/2005JE002584>.
- Morris, R.V., Klingelhofer, G., Schroder, C., Fleischer, I., Ming, D., Yen, A.S., Gellert, R., Arvidson, R.E., Rodionov, D.S., Crumpler, L.S., Clark, B.C., Cohen, B.A., McCoy, T.J., Mittlefehldt, D.W., Schmidt, M.E., de Souza, P.A., Squyres, S.W., 2008. Iron mineralogy and aqueous alteration from Husband Hill through Home Plate at Gusev Crater, Mars: results from the Mossbauer instrument on the Spirit Mars Exploration Rover. *Journal of Geophysical Research* 113, E12S42. <http://dx.doi.org/10.1029/2008JE003201>.
- Nordstrom, D.K., 2009. Acid rock drainage and climate change. *Journal of Geochemical Exploration* 100, 97–104.
- Nordstrom, D.K., Alpers, C.N., 1999. Negative pH, efflorescent mineralogy, and consequences for environmental restoration at the Iron Mountain superfund site, California. *Proceedings of the National Academy of Science USA* 96, 3455–3462.
- Parkinson, K.J., Day, W., 1981. Water vapor calibration using salt hydrate transitions. *Journal of Experimental Botany* 32, 411–418.
- Peterson, R.C., 2011. Cranswickite $\text{MgSO}_4 \cdot 4\text{H}_2\text{O}$, a new mineral from Calingasta, Argentina. *American Mineralogist* 96, 869–877.
- Peterson, R.C., Grant, A., 2005. Dehydration and crystallization reactions of secondary sulfate minerals found in mine waste: in situ powder diffraction experiments. *Canadian Mineralogist* 43, 1173–1181.
- Peterson, R.C., Wang, R., 2006. Crystal molds on Mars: melting of a possible new mineral species to create Martian chaotic terrain. *Geology* 34, 957–960.
- Peterson, R.C., Nelson, W., Madu, B., Shurvell, H.F., 2007. Meridianite: a new mineral species observed on Earth and predicted to exist on Mars. *American Mineralogist* 92, 1756–1759.
- Piatak, N.M., Seal II, R.R., Hammarstrom, J.M., 2004. Mineralogical and geochemical controls on the release of trace elements from slag produced by base- and precious-metal smelting at abandoned mine sites. *Applied Geochemistry* 19, 1039–1064.
- Plummer, L.N., Parkhurst, D.L., Fleming, G.W., Dunkle, S.A., 1988. U.S. Geological Survey Water-Resources Investigation Report 88–4153: A Computer Program Incorporating Pitzer's Equations for Calculation of Geochemical Reactions in Brines. U.S. Geological Survey, Reston, VA.
- Polyanskii, N.G., Gorbunov, G.V., Polyanskaya, N.L., 1976. Methods of Studying Ion-Exchange Resins. *Izdatelstvo Khimii, Moscow*.
- Posnjak, E., Merwin, H., 1922. The system, $\text{Fe}_2\text{O}_3\text{-SO}_3\text{-H}_2\text{O}$. *Journal of American Chemical Society* 44, 1965–1994.
- Pytkowicz, R.M., 1979. Activity coefficients in electrolyte solutions. In: Pitzer, K.S. (Ed.), *Activity Coefficients in Electrolyte Solutions*, second ed. CRC Press, Boca Raton.
- Rimstidt, J.D., Vaughan, D.J., 2003. Pyrite oxidation: a state-of-the-art assessment of the reaction mechanism. *Geochimica et Cosmochimica Acta* 67, 873–880.
- Roach, L.H., Mustard, J.F., Murchie, S.L., Bibring, J.P., Forget, F., Lewis, K.W., Aharonson, O., Vincendon, M., Bishop, J.L., 2009. Testing evidence of recent hydration state change in sulfates on Mars. *Journal of Geophysical Research* 114, E00D02. <http://dx.doi.org/10.1029/2008JE003245>.
- Roach, L.H., Mustard, J.F., Lane, M.D., Bishop, J.L., Murchie, S.L., 2010a. Diagenetic haematite and sulfate assemblages in Valles Marineris. *Icarus* 207, 659–674.
- Roach, L.H., Mustard, J.F., Swayze, G., Milliken, R.E., Bishop, J.L., Murchie, S.L., Lichtenberg, K., 2010b. Hydrated mineral stratigraphy of Ius Chasma, Valles Marineris. *Icarus* 206, 253–268.
- Robinson, P.D., Fang, J.H., 1973. Crystal-structures and mineral chemistry of hydrated ferric sulfates. III. Crystal-structure of kornelite. *American Mineralogist* 58, 535–539.
- Rodgers, K.A., Hamlin, K.A., Browne, P.R.L., Campbell, K.A., Martin, R., 2000. The steam condensate alteration mineralogy of Ruatapu cave, Orakei Korako geothermal field, Taupo Volcanic Zone, New Zealand. *Mineralogical Magazine* 64, 125–142.
- Romero, A., González, I., Galán, E., 2006. The role of efflorescent sulfates in the storage of trace elements in stream waters polluted by acid mine-drainage; the case of Peña del Hierro, southwestern Spain. *Canadian Mineralogist* 44, 1431–1446.
- Rye, R.O., 2005. A review of the stable-isotope geochemistry of sulfate of minerals in selected igneous environments and related hydrothermal systems. *Chemical Geology* 215, 5–36.
- Sánchez España, J., López Pamo, E., Santofimia, E., Aduvire, O., Reyes, J., Baretino, D., 2005. Acid mine drainage in the Iberian Pyrite Belt (Odiel river watershed, Huelva, SW Spain). *Applied Geochemistry* 20, 1320–1356.
- Savijärvi, H., 1995. Mars boundary layer modeling: diurnal moisture cycle and soil properties at the Viking Lander 1 site. *Icarus* 17, 120–127.
- Seal, R.R., II, Hammarstrom, J.M., 2003. Geoenvironmental models of mineral deposits: Examples from massive sulfide and gold deposits. In: Jambor, J.L., Blowes, D.W., Ritchie, A.I.M., (Eds.), *Environmental Aspects of Mine Wastes*, Mineralogical Association of Canada Short Course Series 31, pp. 11–50.
- Seal II, R.R., Hammarstrom, J.M., Johnson, A.N., Piatak, N.M., Wandless, G.A., 2008. Environmental geochemistry of a Kuroko-type massive sulfide deposit at the abandoned Valzinco mine, Virginia, USA. *Applied Geochemistry* 23, 320–342.
- Schumb, W.C., 1923. The dissociation pressures of certain salt hydrates by the gas-current saturation method. *Journal of the American Chemical Society* 45, 342–354.
- Smith, M.D., 2002. The annual cycle of water vapor on Mars as observed by the thermal emission spectrometer. *Journal of Geophysical Research* 107 (E11), 5115. <http://dx.doi.org/10.1029/2001JE001522>.
- Smith, M.D., Wolff, M.J., Lemmon, M.T., Spanovich, N., Banfield, D., Budney, C.J., Clancy, R.T., Ghosh, A., Landis, G.A., Smith, P., Whitney, B., Christensen, P.R., Squyres, S.W., 2004. First atmospheric science results from the Mars exploration rovers Mini-TES. *Science* 306, 1750–1753.
- Smith, M.D., Wolff, M.J., Spanovich, N., Ghosh, A., Banfield, D., Christensen, P.R., Landis, G.A., Squyres, S.W., 2006. One Martian year of atmospheric observations using MER Mini-TES. *Journal of Geophysical Research* 111, E12S13. <http://dx.doi.org/10.1029/2006JE002770>.
- Smuda, J., Dold, B., Spangenberg, J.E., Pfeifer, H.-R., 2008. Geochemistry and stable isotope composition of fresh alkaline porphyry copper tailings: implications on

- sources and mobility of elements during transport and early stages of deposition. *Chemical Geology* 256, 62–76.
- Spanovich, N., Smith, M.D., Smith, P.H., Wolff, M.J., Christensen, P.R., Squyres, S.W., 2006. Surface and near-surface atmospheric temperatures for the Mars Exploration Rover landing sites. *Icarus* 180, 314–320.
- Squyres, S.W., Grotzinger, J.P., Arvidson, R.E., Bell III, J.F., Calvin, W., Christensen, P.R., Clark, B.C., Crisp, J.A., Farrand, W.H., Herkenhoff, K.E., Johnson, J.R., Klingelhofer, G., Knoll, A.H., McLennan, S.M., McSween Jr., H.Y., Morris, R.V., Rice Jr., J.W., Rieder, R., Soderblom, L.A., 2004. In situ evidence for an ancient aqueous environment at Meridiani Planum, Mars. *Science* 306, 1709–1714.
- Srebrodolskiy, B.I., 1977. Products of melanterite alteration. *Dopovidi Akademii nauk Ukrainської RSR Seriya B* 39, 797–800 (in Ukrainian).
- Tosca, N.S., Smirnov, A., McLennan, S.M., 2007. Application of the Pitzer ion interaction model to isopiestic data for the $\text{Fe}_2(\text{SO}_4)_3\text{-H}_2\text{SO}_4\text{-H}_2\text{O}$ system at 298.15 and 323.15 K. *Geochimica Cosmochimica Acta* 71, 2680–2698.
- Tuttle, M.L.W., Breit, G.N., Goldhaber, M.B., 2009. Weathering of the New Albany Shale, Kentucky: II Redistribution of minor and trace elements. *Applied Geochemistry* 24, 1565–1578.
- Valente, T.M., Leal Gomes, C., 2008. Occurrence, properties and pollution potential of environmental minerals in acid mine drainage. *Science of the Total Environment* 407, 1135–1152.
- Vaniman, D.T., Bish, D.L., Chipera, S.J., Fialips, C.I., Carey, J., Feldman, W., 2004. Magnesium sulphate salts and the history of water on Mars. *Nature* 431, 663–665.
- Vaniman, D.T., Chipera, S.J., 2006. Transformation of Mg- and Ca-sulfate hydrates in Mars regolith. *American Mineralogist* 91, 1628–1642.
- Vaniman, D.T., Bish, D.L., Chipera, S.J., 2009. Bassanite on Mars. Abstract #1654 for XXXVIIIth Lunar and Planetary Sciences Conference.
- van't Hoff, J.H. et al., 1912. Untersuchungen über die Bildungsverhältnisse der ozeanischen Salzablagerungen insbesondere des Stassfurter Salzlagers. *Akademsche Verlagsgesellschaft m.b.H.*, Leipzig.
- Vicenzi, E.P., Fries, M., Fahey, A., Rost, D., Greenwood, J.P., Steele, A., 2007. Detailed elemental, mineralogical, and isotopic examination of jarosite in martian meteorite MIL 03346. *Lunar and Planetary Science Conference XXXVIII*, Abstract 2335.
- Wagman, D.D., Evans, W.H., Parker, V.B., Schumm, R.H., Halow, I., Bailey, S.M., Churney, K.L., Nuttal, R.L., 1982. The NBS tables of chemical thermodynamic properties: selected values for inorganic and C_1 and C_2 organic substances in SI units. *Journal of Physical Chemistry Reference Data* 11 (Suppl. 2), 392.
- Wang, A., 2012. Subsurface hydrous salts and obliquity cycle on Mars. Abstract #2172 for 43rd Lunar and Planetary Science Conference.
- Wang, A., Freeman, J.J., Jolliff, B.L., Chou, I.M., 2006. Sulfates on Mars: a systematic Raman spectroscopic study of hydration states of magnesium sulfates. *Geochimica et Cosmochimica Acta* 70, 6118–6135.
- Wang, A., Bell, J., Li, R., Johnson, J., Farrand, W., Cloutis, E.A., Arvidson, R.E., Crumpler, L., Squyres, S.W., McLennan, S.M., Herkenhoff, K.E., Ruff, S.W., Knudson, A.T., Chen, W., Greenberger, R., 2008. Light-toned salty soils and coexisting Si-rich species discovered by the Mars Exploration Rover Spirit in Columbia Hills. *Journal of Geophysical Research* 113, E12S40. <http://dx.doi.org/10.1029/2008JE003126>.
- Wang, A., Freeman, J.J., Jolliff, B.L., 2009. Phase transition pathways of the hydrates of magnesium sulfate in the temperature range 50 °C to 5 °C: implication for sulfates on Mars. *Journal of Geophysical Research* 114, E04010. <http://dx.doi.org/10.1029/2008JE003266>.
- Wang, A., Ling, Z.C., 2011. Ferric sulfates on Mars: a combined mission data analysis of salty soils at Gusev crater and laboratory experimental investigations. *Journal of Geophysical Research* 116, E00F17. <http://dx.doi.org/10.1029/2010JE003665>.
- Wang, A., Freeman, J.J., Chou, I.-M., Jolliff, B.L., 2011. Stability of Mg-sulfates at -10 °C and the rates of dehydration/rehydration processes under Mars relevant conditions. *Journal of Geophysical Research* 116, E12006. <http://dx.doi.org/10.1029/2011JE003818>.
- Wang, A., Ling, Z.C., Freeman, J.J., 2012a. Stability field and phase transition pathways of hydrous ferric sulfates in the temperature range 50 °C to 5 °C: implication for Martian sulfates. *Icarus* 218, 622–643. <http://dx.doi.org/10.1016/j.icarus.2012.01.003>.
- Wang, A., Feldman, W.C., Mellon, M.T., Mianping Zheng, M.P., 2012b. Preservation of subsurface sulfates with mid-to-high degree of hydration in equatorial regions on Mars. Abstract #1482635 for 2012 Fall AGU.
- Wentworth, S.J., Gooding, J.L., 1993. Weathering features and secondary minerals in Antarctic shergottites ALHA77005 and LEW88516. *Lunar and Planetary Science Conference XXIV*, pp. 1507–1508.
- Wentworth, S.J., Gooding, J.L., 1994. Carbonates and sulfates in the Chassigny meteorite: further evidence for aqueous chemistry on the SNC meteorite planet. *Meteoritics* 29, 860–863.
- Wentworth, S.J., Gooding, J.L., 1996. Water-based alteration of the martian meteorite, QUE94201, bisulfate-dominated solutions. *Lunar and Planetary Science Conference XXVII*, pp. 1421–1422.
- Wentworth, S.J., Thomas-Keptra, K.L., McKay, D.S., 2000. Weathering and secondary minerals in the martian meteorite Shergotty. *Lunar and Planetary Science Conference XXXI*, Abstract 1888.
- Wentworth, S.J., Thomas-Keptra, K.L., McKay, D.S., 2002. Water on Mars: Petrographic evidence. *Lunar and Planetary Science Conference XXXIII*, Abstract 1932.
- Whittig, L.D., Deyo, A.E., Tanji, K.K., 1982. Evaporite mineral species in Mancos shale and salt efflorescence, upper Colorado River basin. *Soil Science Society of America Journal* 46, 645–651.
- Xu, W.Q., Tosca, N.J., McLennan, S.M., Parise, J.B., 2009. Humidity-induced phase transitions of ferric sulfate minerals studied by in situ and ex situ X-ray diffraction. *American Mineralogist* 94, 1629–1637.
- Yakhontova, L.K., Dvurechenskaya, S.S., Sandomirskaya, S.M., Sergeeva, N.E., Pal'chik, N.A., 1988. Sulfates from the cryogenic supergene zone: first finds: Nomenclature problems. *Mineral Zhurnal* 10, 3–15.
- Zimbelman, D.R., Rye, R.O., Breit, G.N., 2005. Origin of sulfate minerals in active andesitic stratovolcanoes. *Chemical Geology* 215, 37–60.
- Zodrow, E.L., Wiltshire, J., McCandlish, K., 1979. Hydrated sulfates in the Sydney coalfield of Cape Breton, Nova Scotia. II. Pyrite and its alteration products. *Canadian Mineralogist* 17, 63–70.